



Impact of channel selection on SST retrievals from passive microwave observations

Nielsen-Englyst, Pia; Høyer, Jacob L.; Alerskans, Emy; Pedersen, Leif Toudal; Donlon, Craig

Published in:
Remote Sensing of Environment

Link to article, DOI:
[10.1016/j.rse.2020.112252](https://doi.org/10.1016/j.rse.2020.112252)

Publication date:
2021

Document Version
Publisher's PDF, also known as Version of record

[Link back to DTU Orbit](#)

Citation (APA):
Nielsen-Englyst, P., Høyer, J. L., Alerskans, E., Pedersen, L. T., & Donlon, C. (2021). Impact of channel selection on SST retrievals from passive microwave observations. *Remote Sensing of Environment*, 254, Article 112252. <https://doi.org/10.1016/j.rse.2020.112252>

General rights

Copyright and moral rights for the publications made accessible in the public portal are retained by the authors and/or other copyright owners and it is a condition of accessing publications that users recognise and abide by the legal requirements associated with these rights.

- Users may download and print one copy of any publication from the public portal for the purpose of private study or research.
- You may not further distribute the material or use it for any profit-making activity or commercial gain
- You may freely distribute the URL identifying the publication in the public portal

If you believe that this document breaches copyright please contact us providing details, and we will remove access to the work immediately and investigate your claim.



Impact of channel selection on SST retrievals from passive microwave observations

Pia Nielsen-Englyst^{a,b,*}, Jacob L. Høyer^b, Emy Alerskans^{c,b}, Leif Toudal Pedersen^a, Craig Donlon^d

^a DTU-Space, Technical University of Denmark, DK-2800 Lyngby, Denmark

^b Danish Meteorological Institute, Lyngbyvej 100, DK-2100 Copenhagen Ø, Denmark

^c University of Copenhagen, Tagensvej 16, DK-2200 København N, Denmark

^d European Space Agency/European Space Research and Technology Centre (ESA/ESTEC), 2201 AZ Noordwijk, the Netherlands

ARTICLE INFO

Keywords:

Remote sensing
Passive microwaves
Channel selection
Copernicus imaging microwave radiometer (CIMR)
AMSR-E
Sea surface temperature (SST)
Optimal estimation (OE)

ABSTRACT

Two retrieval algorithms developed as a part of the European Space Agency Climate Change Initiative (ESA-CCI) project are used to assess the effects of withholding observations from selected frequency channels on the retrieved subskin Sea Surface Temperature (SST) from AQUA's Advanced Microwave Scanning Radiometer—Earth Observing System (AMSR-E) and to evaluate a Copernicus Imaging Microwave Radiometer (CIMR) like channel configuration.

The first algorithm is a statistical regression-based retrieval algorithm, while the second is a physically based optimal estimation (OE) algorithm. A database with matching satellite and drifting buoy observations is used to test the performance of each channel configuration using both retrieval algorithms to identify the most optimal channel selection for accurate SST retrievals. The evaluation against in situ observations allows identification of the strengths and weaknesses of the two retrieval algorithms, and demonstrates the importance of using in situ observations to evaluate existing theoretical retrieval uncertainty studies. Overall, the performance increases as expected when more channels are included in the retrieval. In particular, more channels allow a better performance for the range of different observing conditions (e.g. cold waters). The two retrieval algorithms agree that for a three-channel configuration, the 6, 10, 18 GHz (V and H polarization) is better than the 6, 10, 23 GHz configuration (V and H polarization). This is demonstrated for different geographical regions and throughout all seasons. Of the different combinations tested here, it is evident that withholding observations from the 23 and 36 GHz channels from the retrieval has the least impact on the SST performance. Overall, this analysis shows that the CIMR like channel configuration performs very well when compared to an AMSR-E like constellation using both retrieval algorithms.

1. Introduction

Global sea surface temperature (SST) observations are crucial for climate monitoring (e.g. Merchant et al., 2019), numerical weather prediction (NWP; Brasnett and Colan, 2016; Chelton and Wentz, 2005), ocean and coupled models (Liang et al., 2017; Le Traon et al., 2015; Yang et al., 2015) and in understanding and predicting the state of the ocean and the atmosphere (Gentemann et al., 2003; Monzikova et al., 2017; Ning et al., 2018; O'Carroll et al., 2019). Global sampling of SST is only possible through satellite remote sensing, and SST was one of the first ocean variables to be observed from earth observing satellites (see

e.g. Minnett et al. (2019) for a detailed overview of the latest progress in satellite SST retrievals). SST has been derived from infrared (IR) satellite observations since 1981, with a typical spatial resolution of 1–4 km (Embury et al., 2012; Gladkova et al., 2016; Merchant et al., 2019; Reynolds et al., 2002). However, the IR observations are biased from aerosols and the temporal/spatial sampling is problematic in regions with persistent cloud cover (such as the Polar and Tropical regions), since IR wavelengths are unable to observe the surface through clouds (Merchant et al., 1999, 2006; Vázquez-Cuervo et al., 2004).

Observations from passive microwave (PMW) sensors are important alternatives to IR observations as PMW measurements are not prevented

* Corresponding author at: DTU-Space, Technical University of Denmark, DK-2800 Lyngby, Denmark.

E-mail address: pne@dmi.dk (P. Nielsen-Englyst).

<https://doi.org/10.1016/j.rse.2020.112252>

Received 28 April 2020; Received in revised form 26 November 2020; Accepted 9 December 2020

Available online 25 December 2020

0034-4257/© 2020 The Author(s).

Published by Elsevier Inc.

This is an open access article under the CC BY-NC-ND license

(<http://creativecommons.org/licenses/by-nc-nd/4.0/>).

by non-precipitating clouds or biased by aerosols (Donlon et al., 2007, 2010; Ulaby et al., 1981; Wentz et al., 2000). The first space borne microwave radiometer capable of measuring SST was the Scanning Multichannel Microwave Radiometer (SMMR) carried on Seasat 1 and Nimbus 7, both launched in 1978 (Lipes, 1982; Milman and Wilheit, 1985). However, SST retrievals from Nimbus-7 SMMR suffered from significant calibration problems, resulting in SST errors as high as 1.12 °C (Milman and Wilheit, 1985) as well as very coarse spatial resolution of approx. 150 km, limiting its usefulness. The high quality PMW SST record began in 1997 after the launch of the Tropical Rainfall Measuring Mission (TRMM) Microwave Imager (TMI; e.g. Kummerow et al., 1998; Wentz, 2015; Wentz et al., 2000) (10 GHz channel), which provided SST observations from 1998 to 2014 between 40°N/S. The TRMM mission was followed by the Global Precipitation Mission (GPM) Microwave Imager (GMI; Bidwell et al., 2005; Draper et al., 2015), which was launched in 2014, and uses a larger antenna compared to TMI resulting in a better spatial resolution. The first global PMW SST data became available in 2002 by AQUA's Advanced Microwave Scanning Radiometer – Earth Observing System (AMSR-E; e.g. Chelton and Wentz, 2005; Kawanishi et al., 2003), using the channels at 6 GHz. The instrument ceased normal operations in October 2011 and was followed by the currently flying Advanced Microwave Radiometer 2 (AMSR2), flown on the Global Change Observing Mission 1st – Water (GCOM-W1), which was launched in 2012 (Imaoka et al., 2010). AMSR2 has a larger antenna compared to AMSR-E, which provides improved spatial resolution and the additional channel at 7 GHz allows for better identification of Radio Frequency Interference (RFI). PMW SST estimates using the 6.9 and 10.7 GHz channels have a typical spatial sampling of about 10 km, a resolution of 50–60 km and an uncertainty of about 0.4 °C (Gentemann, 2014; Gentemann et al., 2010; Nielsen-Englyst et al., 2018; Wentz et al., 2000). The uncertainty is mainly attributed to mismatches in time and space of observations, differences in measurement depth, and errors in satellite estimates and in situ observations.

The current microwave imagers do not capture the subscale to mesoscale variability and are contaminated near (~100 km) coasts and in the marginal ice zone at the 6.9 GHz channels, due to the large field of view (e.g. AMSR2 has a 64 × 32 km field of view at 6.9 GHz). The spatial resolution of SST retrievals is limited by the ratio of the wavelength of measurement to the antenna diameter, the satellite altitude and the incidence angle (Wentz and Meissner, 2000). A larger antenna is therefore required to obtain a high spatial resolution (e.g. for a resolution of ~10 km at 10 GHz an antenna of ~6 m is required assuming a satellite altitude of 830 km). Improving the spatial resolution of the measurements obtained by the 6.9 and 10.7 GHz channels could lead to substantial improvements of PMW SST estimates and their information content in global products and regional analysis systems.

A sustained continuity of PMW imagers, which can provide measurements at higher spatial resolution and with high radiometric fidelity to retrieve SSTs that meet the current operational needs, is a major concern within the SST community (O'Carroll et al., 2019). The Chinese Microwave Radiometer Imager onboard the HaiYang-2B (HY-2B) is a future PMW mission with a 6.9 GHz channel (Zhang et al., 2020), while the FengYun-3 series (FY-3D and FY-3F) also has a 10.65 GHz channel. However, their spatial resolutions are three times lower compared to AMSR2. In addition, the AMSR2 follow-on mission (AMSR3) is officially approved as a project to be installed on the Global Observation SATellite for Greenhouse gases and Water Cycle (GOSAT-GW) to be launched in 2023 by JAXA (Hirabayashi, 2020). AMSR3 will be of almost equivalent capability to that of AMSR2, but with addition of high-frequency channels (166 and 183 GHz) (Hirabayashi, 2020).

A new radiometer, the Copernicus Imaging Microwave Radiometer (CIMR), is currently being studied by the European Space Agency (ESA) for the Copernicus Expansion program of the European Union (<http://www.cimr.eu/>). CIMR is a polar mission, designed to observe all-weather, high-resolution, high-accuracy, sub-daily observations of SST and sea ice as the primary variables (Donlon, 2019). It is the

intention to include the radiometer channels 6.9, 10.7, 18.7 and 36.6 GHz common with AMSR-E and AMSR2, but also the 1.4 GHz channel, providing continuity to the current Soil Moisture and Ocean Salinity (SMOS; Kerr et al., 2010) and the Soil Moisture Active Passive (SMAP; Fore et al., 2016) missions. The anticipated spatial resolution of CIMR is shown in Table 1 and compared to the spatial resolution of AMSR-E. The higher spatial resolution at the lower frequency channels enables retrievals of SST and other surface parameters at a higher resolution and lower uncertainty than possible with the current missions.

Studies have been conducted to assess the expected impact of CIMR observations on retrievals and applications for: sea ice, snow depth and sea surface salinity (Braakmann-Folgmann and Donlon, 2019; Ciani et al., 2019; Scarlat et al., 2020). Theoretical information content studies have been made with the aim of identifying the role of different channel combinations and the expected CIMR performance for SST (Kilic et al., 2018, 2019; Pearson et al., 2018, 2019; Prigent et al., 2013). Kilic et al. (2018) derive a mean global SST retrieval uncertainty of 0.2 °C at a spatial resolution of 15 km using the intended CIMR channel configuration, which is a clear improvement in performance compared to AMSR2. They also show that the estimated CIMR retrieval uncertainty varies strongly with SST (from 0.15 °C for warm SSTs and up to 0.45 °C for cold SSTs) and wind speed (larger uncertainties for higher wind speeds), but is only weakly impacted by the total column water vapor content and total cloud liquid water content. However, a comparison of the theoretical retrieval error standard deviations obtained for AMSR2 by Kilic et al. (2018) (Figs. 5 and 6) and the standard deviations of retrieved versus drifting buoy SSTs in Alerskans et al. (2020) (Figs. 7 and 8) shows significant differences between the theoretical and the observed uncertainties. These differences can arise due to the different retrieval methods (physical versus statistical) or due to limitations in the forward models ability to simulate the real conditions. Kilic et al. (2019) compared some of the ocean forward models used in the theoretical studies and found large differences between the models and significant disagreement with observations, in particular for high wind speeds and cold SSTs.

With the discrepancies among the forward models, it is thus important to apply several types of retrieval algorithms for different channel configurations and to evaluate them against a common in situ reference data set to supplement the existing theoretical studies. The aim of this study is to determine the impact of using different channel selections on retrieved SST and to assess the realistic performances of a physically based optimal estimation (OE) algorithm and a statistical regression (RE) based algorithm against in situ observations. The use of in situ observations can inform us about deficiencies and strengths of different types of retrieval algorithms as well as evaluate the impact of different channel combinations. In addition to the preparation for the CIMR mission, it is also important to investigate the effects of different channel combinations in a realistic scenario, where future ITU frequency allocations may contaminate some of the specific frequency bands used for PMW observations of the ocean. Furthermore, this study can also be used to assess the impact during an instrument failure, where the detector or electronics for one or several channels fail during operations. Finally, the results can aid in the construction of long-term climate data records (CDRs) and harmonization of PMW satellite missions with

Table 1
The frequency channels of the AMSR-E and CIMR mission and their respective spatial resolutions.

Frequency (GHz)		1.4	6.9	10.6	18.7	23.8	36.5	89.0
Spatial Resolution (3 dB footprint size) (km x km)	AMSR-E	–	75	51 × 29	27 × 16	32 × 18	14 × 8	6 × 4
	CIMR	64	19	13 × 7	6 × 4	–	5 × 3	–
		36	11					

different channel configurations.

For the investigations conducted here, a physical and a statistical retrieval algorithm will be applied, where the physically based algorithm is a type of retrieval algorithm similar to the ones used for the information content studies (Kilic et al., 2018, 2019; Pearson et al., 2018; Prigent et al., 2013) and the statistical algorithm resembles the retrievals currently used to generate many existing PMW satellite SST products (Alerskans et al., 2020; Chang et al., 2015; Gentemann et al., 2010; Shibata, 2006; Wentz and Meissner, 2007).

The two different retrieval algorithms used here are developed within the ESA Climate Change Initiative (CCI) for SST (Merchant et al., 2014). The first algorithm is an optimal estimation algorithm (Nielsen-Englyst et al., 2018), which inverts a forward model to retrieve different geophysical parameters including SST from AMSR-E observations. The second retrieval algorithm is a purely statistical retrieval, consisting of a regression model, which retrieves wind speeds and SSTs using AMSR brightness temperatures (Alerskans et al., 2020). In this study, we test different subsets of the channels available in AMSR-E, which means that we do not consider the 1.4 GHz channels, the actual noise equivalent differential temperatures (NEdT) from CIMR and the higher spatial footprints. However, the results give valuable insight to the relative performance of the different channel combinations, and the differences between the two different types of retrieval algorithms for real conditions using a well-known instrument. This study is therefore an important extension to existing theoretical studies that investigate and prepare for new PMW missions like the CIMR.

The paper is structured such that Section 2 includes a description of the matchup database used for algorithm development and validation. The retrieval algorithms are described in Section 3.1 while Section 3.2 describes the different channel selections and filters, which have been tested. The retrieval results from using different channel selections in both retrieval algorithms are presented in Section 4. Section 5 contains a discussion and Section 6 presents recommendations for future work. Finally, conclusions are given in Section 7.

2. Data

2.1. ESA CCI multisensor matchup dataset (MMD)

This work is built on the ESA CCI Multi-sensor Matchup Dataset (MMD), which is described and used in Nielsen-Englyst et al. (2018) and Alerskans et al. (2020). It includes brightness temperatures from the Level 2A (L2A) swath data product AMSR-E V12 (Ashcroft and Wentz, 2013), with the spatial resampling to the 6.9 GHz resolution (75×43 km). The L2A AMSR-E V12 product also includes a satellite scan quality flag, channel quality flags and the incidence- and azimuth angles. The brightness temperatures have been matched with quality controlled in situ measurements from the International Comprehensive Ocean-Atmosphere Dataset (ICOADS) version 2.5.1 (Woodruff et al., 2011), the Met Office Hadley Centre (MOHC) Ensembles dataset version 4.2.0 (EN4; Good et al., 2013) by requiring a maximal geodesic distance of 20 km and a maximal time difference of 4 h. The 20 km was chosen to ensure that the in situ measurement is located within an AMSR-E footprint, while the maximal time difference balances the need for accurate collocated data with the need for a sufficient number of useable matches. The MMD also includes SST, Total Column Water Vapor (TCWV), Total Cloud Liquid Water (TCLW), and Wind Speed (WS) information from the ERA-Interim (ERA-I) reanalysis data (Dee et al., 2011). For sea surface salinity (SSS), we have included data from the GLOBAL-REANALYSIS-PHY-001-030 reanalysis product provided by the Copernicus Marine Environment Monitoring Service (CMEMS; <http://marine.copernicus.eu>).

The MMD has been filtered for erroneous satellite, in situ and auxiliary data. Erroneous satellite measurements include those contaminated by precipitation and RFI from ground-based sources, geostationary satellites and communication satellites that are identified

and flagged in order to obtain accurate SST retrievals (e.g. Gentemann and Hilburn, 2015). Low quality AMSR-E pixels and brightness temperatures outside the accepted range (0–320 K) were also flagged as erroneous. In addition, data were flagged if the difference between the measurements in vertical (V) and horizontal (H) polarization for the 18–36 GHz channels was negative. The standard deviations of the 23 and 36 GHz channels (both polarizations) were calculated over a 21×21 subregion surrounding the retrieval pixel and were used to flag low quality data. Low quality in situ data and matchups with an in situ or ERA-I SST outside the accepted range ($-2-34$ °C) were flagged as erroneous. Similar, matchups with ERA-I wind speeds greater than 20 m s^{-1} were flagged. Further checks were included to account for situations where the SST retrievals could be compromised due to land and sea ice contamination, diurnal warming effects, precipitation and sun glitter contamination, and RFI. Land and sea ice contamination was accounted for by using the AMSR-E land/ocean flag and ERA-I sea ice fraction. To avoid diurnal warming effects, daytime matchups with ERA-I wind speeds less than 4 m s^{-1} were removed. Rain contamination was accounted for by removing data if the brightness temperature of the 18 V channel exceeded 240 K. Contamination from sun glitter was accounted for by removing data with sun glint angles below 25 degrees. Potential contamination due to RFI was accounted for by using Table 2 in Gentemann and Hilburn (2015), as well as the observation location (for ground based RFI) and the reflection longitude and latitude (for geostationary RFI). As a last control, a $3\text{-}\sigma$ filter was applied on the ERA-I and in situ SST difference. The number of matchups per latitude band is limited in order to ensure a better balance of data across the different latitude bands. For further details on data filtering see Alerskans et al. (2020).

The focus of this study is the year 2010. To obtain an independent validation data set, the matchups from 2010 were divided into four subsets to accommodate the fact that the regression model (see Section 3.1.2) needs to be trained and afterwards validated on independent data. The first three subsets are used exclusively for the training of the regression model whereas the validation subset is used to validate the results from both retrieval algorithms. For a more detailed description on the division into subsets see Alerskans et al. (2020).

The filtered validation subset consists of 1,514,985 matchups from 2010, which are used to compare the performance of the different channel configurations for both retrieval algorithms. Fig. 1 shows the geographical distribution of the validation subset, with the largest number of matchups in North Atlantic Ocean. There is no significant seasonal variation in the matchup distribution. In Section 3.2, different filters are established to be used during the comparison of different channel configurations.

3. Methods

3.1. Retrieval algorithms

3.1.1. Optimal estimation (OE) retrieval algorithm

The OE algorithm used in this study is based on the retrieval algorithm described in Nielsen-Englyst et al. (2018), which is built upon the forward model described in Wentz and Meissner (2000) that relates the observed top of atmosphere brightness temperatures to the relevant

Table 2

The number of matchups (N) left after filtering and the percentage of matchups removed by each filter. Convergence is also required by F1 + F2.

Filter	N	% Removed
No filter	1,514,985	–
OE convergence passed	1,246,425	18
F1: TB RMSE < 0.25 K	694,473	54
F2: TB RMSE < 0.5 K	1,137,765	25
F3: 3RSTD	1,080,336	29

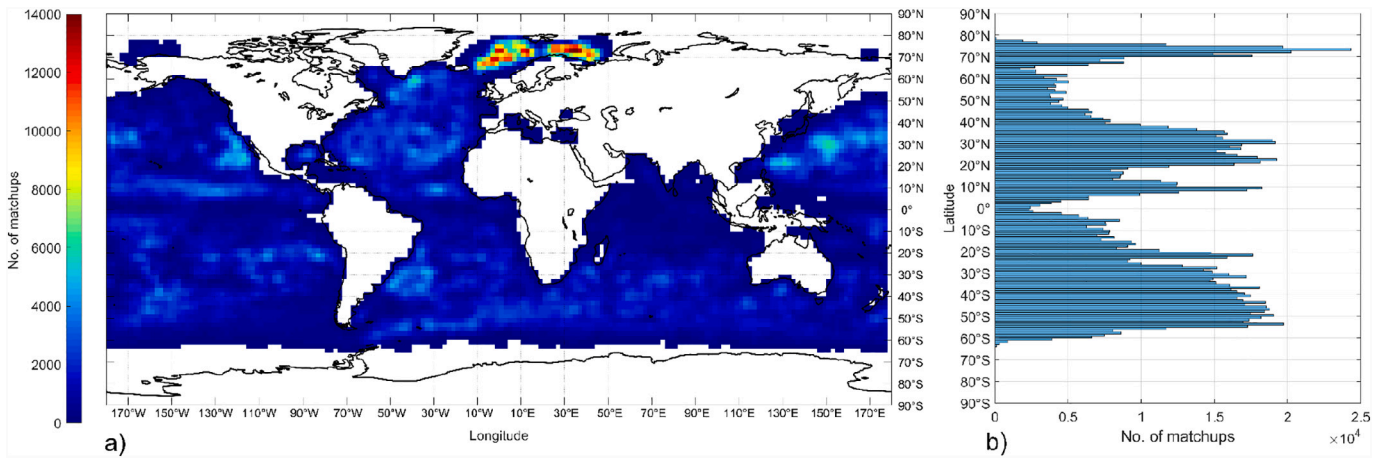


Fig. 1. (a) The geographical distribution of the matchups using a grid size of 5×5 degrees and (b) the latitudinal distribution of matchups, for the filtered validation subset.

geophysical parameters as given by the state vector, $\mathbf{x} = [\text{WS}, \text{TCWV}, \text{TCLW}, \text{SST}]$. These are by experience the most important geophysical parameters influencing the amount of microwave radiation received by the satellite antenna at frequencies in the microwave part of the spectrum over open-ocean (Wentz and Meissner, 2000). Following Nielsen-Englyst et al. (2018), we use a regression model to correct for the forward model residuals, which depends on SST and WS from the previous iteration and the ERA-I wind direction relative to the azimuthal look, φ_r . One way to examine the impact of the different channels on the retrieved parameters is to investigate the change in brightness temperature for a perturbation in the individual geophysical parameters (i.e. the Jacobian matrix). The sensitivity of the brightness temperatures to the geophysical parameters varies with both frequency and polarization. The sensitivity of the forward model to SST is shown in Fig. 2a for the AMSR-E frequencies up to 36 GHz. It illustrates that the sensitivity is larger for the vertical polarizations, where 6.9 V GHz provides the highest sensitivity with maximum changes in brightness temperature of 0.5 K/°C. For 6.9 and in particular the 10.7 GHz, the sensitivity decreases for cold SSTs, indicating that SST retrievals are more difficult in cold waters compared to warm waters. The WS influences the sea surface roughness, which affects the surface emissivity and hence the observed brightness temperatures (Hollinger, 1971; Meissner and Wentz, 2002, 2012). Fig. 2b shows the sensitivity to WS (wind induced surface roughness) with larger sensitivities to horizontal than vertical polarization. There is a distinct change in the slopes at WS of about 7 m s^{-1} where foam starts to form, which increases the emissivity for both polarizations. The effect of water vapor is weak at low frequencies, and peaks at 23 GHz (Fig. 2c). Fig. 2d shows the change in brightness temperature over a range of TCLWs, with the main influence at the 36 GHz channels. The SSS has a small effect and the influence is largest at low frequencies (Fig. 2e). These dependencies are similar to the sensitivities found by Prigent et al. (2013) using the fast radiative transfer model RTTOV, but differ from those found by Pearson et al. (2018). For consistency, the sensitivity to the relative wind direction (φ_r) is shown in Fig. 2f, with the largest impact at the vertical polarizations at angles of 100–250°.

The OE technique presented by Rodgers (2000) has been used to retrieve WS, TCWV, TCLW and SST from AMSR-E observations by inverting the forward model. In the inversion, the forward model is constrained by a priori information about the expected mean and covariance of the geophysical parameters. A priori information from ERA-I has been used for SST, WS, TCWV and TCLW. We use a similar setup as in Nielsen-Englyst et al. (2018), but with an increased diagonal covariance matrix element for SST to increase the sensitivity of the retrieved SST to true changes in SST and to ensure the independency from the first guess SST information from ERA-I. The covariance of the a

priori state \mathbf{x}_a (the a priori guess of the ocean and atmospheric state \mathbf{x}), is therefore given as:

$$\mathbf{S}_a = \begin{bmatrix} e_{WS}^2 & 0 & 0 & 0 \\ 0 & e_{TCWV}^2 & 0 & 0 \\ 0 & 0 & e_{TCLW}^2 & 0 \\ 0 & 0 & 0 & e_{SST}^2 \end{bmatrix} \quad (1)$$

where $e_{WS} = 2 \text{ m s}^{-1}$, $e_{TCWV} = 0.9 \text{ mm}$, $e_{TCLW} = 1 \text{ mm}$ and $e_{SST} = 4 \text{ °C}$. The uncertainties on WS, TCWV and TCLW are best estimates based on available published validation results (Chelton and Freilich, 2005; Dee et al., 2011; Jakobson et al., 2012; Jiang et al., 2012; Li et al., 2008) and the covariances are assumed zero following Nielsen-Englyst et al. (2018). As in Nielsen-Englyst et al. (2018), we use the 5 lower frequencies: 6.9, 10.7, 18.7, 23.8, 36.5 GHz from AMSR-E for the retrieval. The \mathbf{S}_e is listed in Appendix A and the constant bias correction of the forward model ranges from -0.72 K on 10 GHz H to 0.64 K on 18.7 GHz V.

In the OE retrieval method, the error on the retrieval is given by the retrieval error covariance matrix:

$$\mathbf{S} = (\mathbf{S}_a^{-1} + \mathbf{K}_i^T \mathbf{S}_e^{-1} \mathbf{K}_i)^{-1} \quad (2)$$

where \mathbf{K} is the Jacobian of the forward model. The square root of the \mathbf{S} matrix provides the theoretical retrieval error standard deviation. Fig. 3 shows the theoretical retrieval error standard deviation of SST as a function of SST for different WS, TCWV and TCLW conditions using an incidence angle of 55°. The figures show that the theoretical retrieval error is largely dependent on the SST and WS, with largest errors for cold waters and high wind speeds. In comparison, the impact from TCWV and TCLW is very limited. This is in agreement with previous results (Kilic et al., 2018; Prigent et al., 2013).

The OE algorithm also directly provides the sensitivities of the retrieved parameters to the true state through the averaging kernel matrix, which is given by:

$$\mathbf{A}_{ij} = \frac{dx_i}{dx_j} \quad (3)$$

where \mathbf{x}^t is the true state. Using the validation subset as described in Section 2.1 and a filter requiring the root mean squared difference of simulated versus observed brightness temperatures (TB RMSE) less than 0.5 K, the mean sensitivities of the retrieved parameters to the true state are given as: 0.99, 1.00, 1.00 and 0.99 for WS, TCWV, TCLW and SST. The increased sensitivity to SST, compared to the mean value of 0.5 in

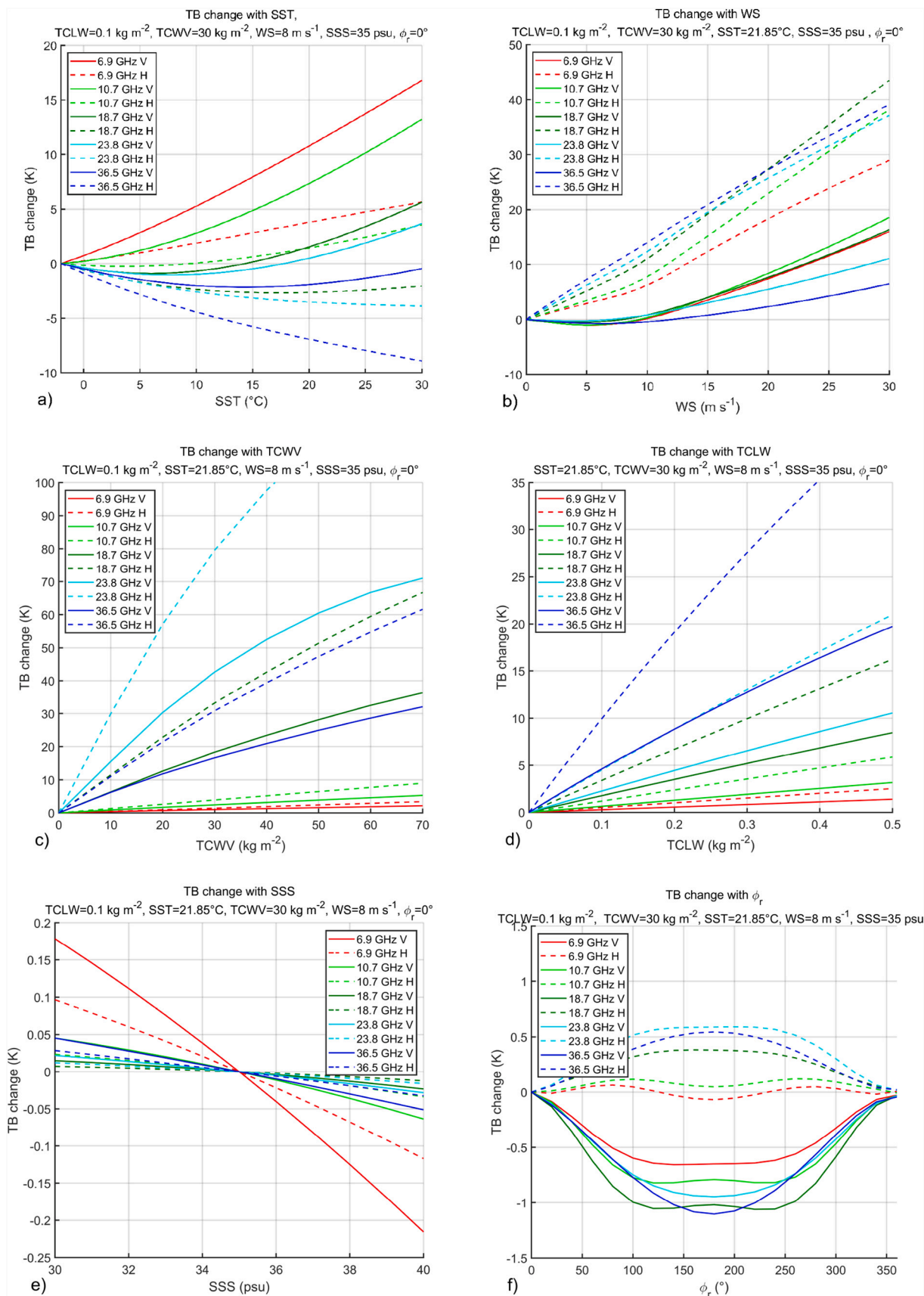


Fig. 2. The change in top-of-atmosphere brightness temperature as a function of a) SST, b) WS, c) TCWV, d) TCLW, e) SSS and f) ϕ_r as simulated by the forward model for the state defined above the individual plots.

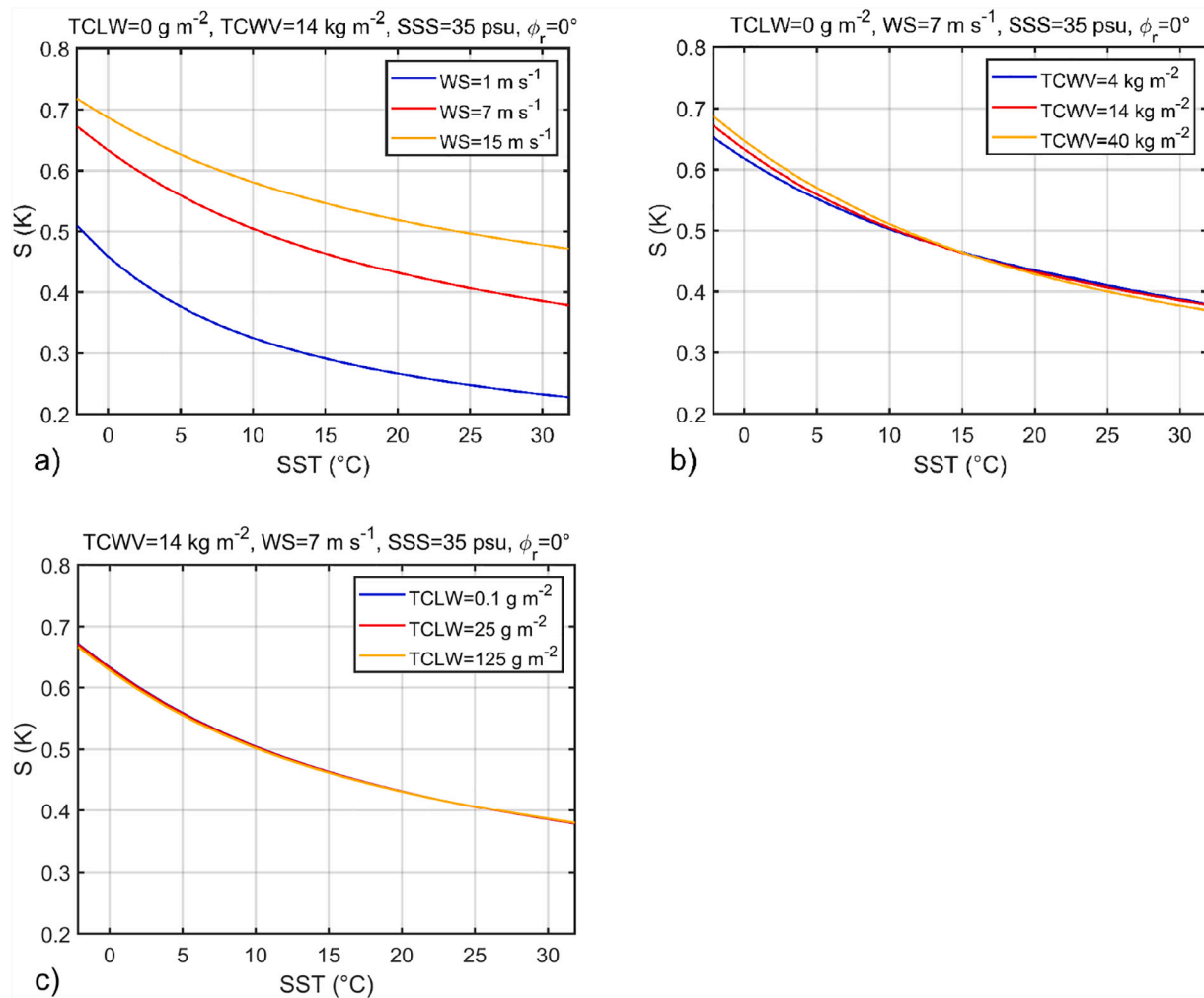


Fig. 3. The simulated retrieval error, S , as a function of SST for different a) WSs, b) TCWVs and c) TCLWs.

Nielsen-Englyst et al. (2018), is a result of the increased uncertainty on the first guess SST from ERA-I. For the same subset (TB RMSE < 0.5 K), the standard deviation of retrieved SST versus in situ observed SST is 0.66 °C.

This setup has been used to run the OE algorithm for a number of different channel selections (see Section 3.2). The forward model simulates brightness temperatures for all channels, but only the selected channels (and the corresponding measurement and forward model uncertainties) are included in the inversion, when different channel combinations are tested.

3.1.2. Regression (RE) model

The statistical retrieval algorithm consists of a two-step WS regression model followed by an SST regression model. Both steps in the WS retrieval algorithm use AMSR-E brightness temperatures, where the first step applies a global algorithm and the second step applies a localized algorithm for fixed WS intervals, using the first-step retrieved WSs. The SST retrieval algorithm applies a global algorithm to retrieve SST using AMSR-E brightness temperatures, the retrieved wind speeds from step two of the WS retrieval algorithm and information from ERA-I. The SST retrieval is very similar to the one described in Alerskans et al. (2020), except that the coefficients are derived globally in this study. Alerskans et al. (2020) used a two-stage retrieval algorithm to retrieve SST, where the first-stage coefficients were derived locally for fixed latitude intervals and ascending and descending passes, respectively, and the second-stage coefficients were derived locally for fixed WS and SST

intervals. The approach with global coefficients was chosen in this study to ensure a consistent comparison of the different channel selections and to minimize effects from localized algorithm coefficient derivations. The global performance of the retrieved SST compared to drifter SST is 0.62 °C using the frequency range 6–36 GHz and a filter of TB RMSE less than 0.5 K, as derived for the OE retrieval (see Section 3.2). In this study, we are considering the relative differences between the different channel selections and we are therefore not concerned with the slightly larger retrieval errors.

3.2. Selection of channels and subsets

Different channel combinations have been tested by selecting different subsets of the channels available in AMSR-E and a configuration where all channels (except the 89 GHz channels) are included. As the focus of this study is SST retrievals, the main focus will be on the 15 different channel selections that all include the 6 GHz channels, as 6 GHz is the primary frequency for global SST retrievals (Wilheit, 1979). However, it is beneficial to know the effect of excluding the 6 GHz channels, as the GMI instrument could be a potential bridging data set between AMSR2 and future PMW missions (Bidwell et al., 2005; Draper et al., 2015). The importance of the 6 GHz channel is clear when the two channel combinations 6, 10, 18, 23 and 36 GHz and 10, 18, 23 and 36 GHz are compared, where the removal of the 6 GHz channels results in an increase in the uncertainty of the retrieved SST from 0.66 °C to 0.75 °C for the OE algorithm and from 0.62 °C to 0.86 °C using the RE

algorithm and the TB RMSE<0.5 K filter.

In this study, we will refer to the AMSR-E channel selection as the one including: 6, 10, 18, 23 and 36 GHz (without the 89 GHz channels), following Nielsen-Englyst et al. (2018). Alerskans et al. (2020) uses the 89 GHz channels, but the inclusion only resulted in slight improvements in the performance. We will refer to the CIMR channel selection as the one including: 6, 10, 18 and 36 GHz (in contrast to the expected configuration, which also includes the 1.4 GHz frequency). It is assumed that the V and H polarizations are always available (or not available) at the same time. In Section 4.1, the 15 different channel selections have been tested on the same validation subset for both the OE and RE retrieval algorithms. It is important to select a suitable selection filter that enables a comparison of the different retrievals. Here, the subsets have been obtained by applying a common filter based on the matchups for which the OE AMSR-E channel configuration has reached convergence and another filter based on TB RMSE also obtained from the OE AMSR-E channel configuration. Differences in the simulated and observed brightness temperatures can usually be attributed to forward model errors or measurement errors (due to e.g. imperfect calibration or channel contamination). Nielsen-Englyst et al. (2018) showed a close relationship between the TB RMSE and the SST retrieval performance. Table 2 shows the number of matchups removed by applying different filters. Of all matchups, 82% reached convergence as defined in Nielsen-Englyst et al. (2018). The next two filters (F1 and F2) include the convergence criterion as well, but also additional filters with TB RMSE less than 0.25 K and 0.5 K, respectively. The F2 filter removes 25% of the matchups (including the ones that did not reach convergence), while the F1 filter removes 54%. Using the simulated brightness temperatures from the AMSR-E channel configuration for filtering will favor this configuration over the other selections, but ensure that the same subset is used for all channel configurations and that the worst retrievals are excluded. The TB RMSE filters have been used in Section 4.1.

In Section 4.2, the analysis focuses on four of the above-mentioned channel configurations: a) 6, 10, 18 GHz, b) 6, 10, 23 GHz, c) 6, 10, 18, 36 GHz, and d) 6, 10, 18, 23, 36 GHz. These configurations have been chosen because they represent the effect of including the 23 GHz channels through a direct comparison against the 18 GHz channels and through a comparison of the CIMR and AMSR-E channel configurations. Furthermore, selection a) and c) allow us to examine the effects of the 36 GHz channels. For this analysis, another filter (F3) has been applied to ensure that the filtering does not favor any of the four channel configurations, and still retains enough matches to make robust validation statistics. The F3 filter removes matchups if the simulated minus observed brightness temperatures exceeds three times the robust standard deviation (3RSTD) for any of the channels in each of the four channel configurations. This filter removes 29% of the matchups, most of which are the same as those removed by the F2 filter, with 99% of the

matchups removed by the F3 filter also removed by the F2 filter. A total of 98% of the matchups removed by the F1 filter are also removed by the F3 filter. Fig. 4 shows the geographical distribution of the removed matchups using the F1 and F3 filter, respectively. Most of removed matchups are located in the areas, where the largest number of matchups is present (see Fig. 1) and the two filters agree on the locations where most matchups are removed.

4. Results

4.1. Performance for all channels

The validation subset (described in Section 2.1) has been used for both retrieval algorithms (RE and OE) to assess the overall impact of using different channel combinations. Fig. 5 shows the robust standard deviation (rstd) of retrieved SST – in situ SST for the OE and RE algorithms, using the 15 different channel combinations, where the F2 and F1 filters have been applied, removing 25% and 54% of the matchups, respectively (see Section 3.2). The channel configurations are ranked from the highest standard deviations to the lowest using the RE model results and the F1 filter to determine the order. This ranking order of the channels will be used for all figures in this section. Adding more channels leads to a better performance of the RE model, with the 6, 10, and 18 GHz channels being the most important. Using the F1 filter improves the RE performance for all channel configurations, with limited changes in the ranking order compared to the F2 filter. The TB RMSE filtering shows improvements in the RE retrieval of comparable magnitude as when using the OE algorithm. This shows the value of the TB RMSE factor as an uncertainty indicator. The OE algorithm shows less variation among the different channel combinations compared to the RE algorithm, and the OE algorithm performs quite well by only including 2 frequencies, where it outperforms the RE algorithm.

The differences and similarities between the RE and OE algorithms have been investigated further by looking at the performance during different weather and surface conditions, using the F2 filter. This filter was chosen to keep sufficient matchups in the different categories and to minimize effects from filtering on the results. Fig. 6a–b show the performance of the retrieved SST for calm or strong winds (calm or rough sea), cold or warm SSTs, and dry or humid conditions for the OE and RE algorithm, respectively. Using 500 bootstrap samples with replacement (same size as N), the average width of the 90% confidence intervals is 0.0030 °C, when considering both algorithms and all the different weather/surface conditions and channel selections. The maximum width of the 90% confidence intervals is 0.0075 °C and calculated for the RE WS > 10 m s⁻¹ and the 6, 18 GHz channel selection data subset. Warm, calm waters and humid conditions show a good and similar performance for the different channel selections for both algorithms.

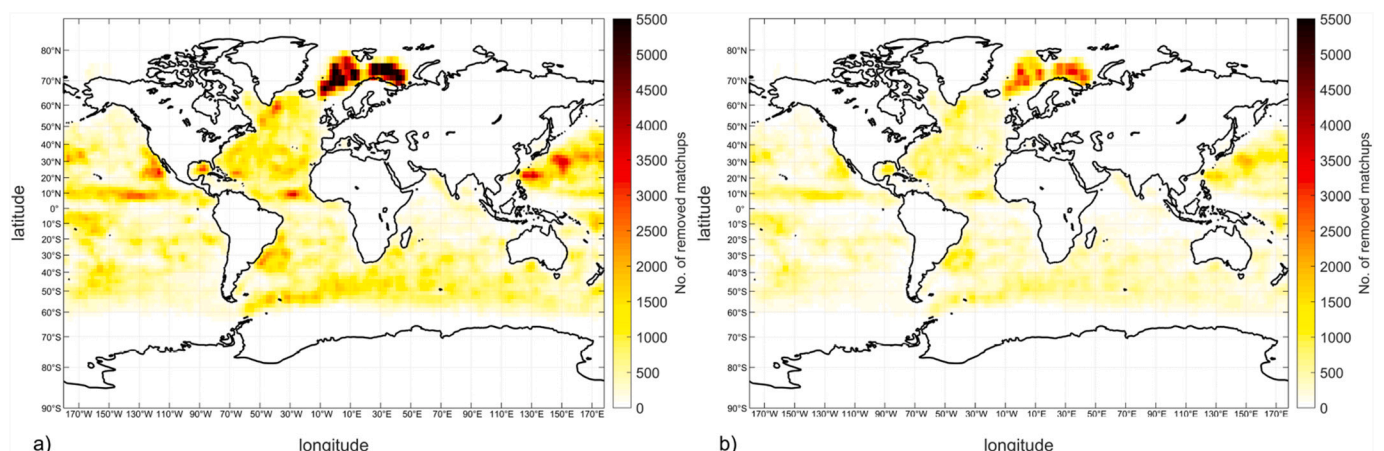


Fig. 4. The number of matchups removed by a) the F1 (TB RMSE<0.25 K) filter and b) the F3 (3RSTD) filter using 5 × 5 degree bins.

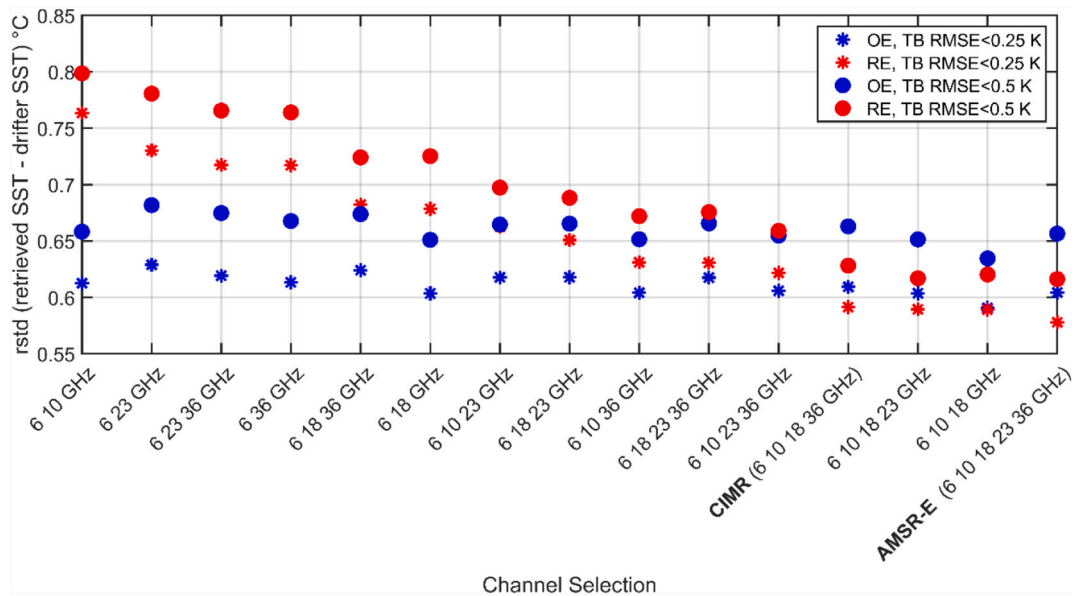


Fig. 5. Robust standard deviation of retrieved SST against drifter SST for different channel selections using the OE and RE algorithm and the filters F1 (TB RMSE < 0.25 K) and F2 (TB RMSE < 0.5 K), respectively. The channel configurations are ranked from the highest to the lowest standard deviations using F1 filtering and the RE algorithm.

Rough and cold waters provide equally high standard deviations, when compared to the relatively low standard deviations observed for warm and calm waters. Both algorithms show a good performance for high TCWV conditions, but this effect is likely related to the good performance in warm waters, with 96% of the high water vapor matchups located in warm waters (>15 °C). By including more channels, the algorithms tend to retrieve better SSTs in cold and rough waters, reducing the overall spread and thus allowing the algorithms to better represent all observing conditions. One of the key differences between the two algorithms is seen in the variability among the different weather and surface conditions. The OE algorithm shows significant increases in uncertainty for cold and rough waters, but a very good performance in warm and calm waters for all channel configurations. In contrast, the RE model shows limited variability among the different weather and surface conditions, especially when more channels are included. This demonstrates the strength of the statistical RE model, which always maximizes the amount of information in the channels available for retrieval based upon the information in the training data. In few of the RE channel combinations (6, 10 GHz and 6, 36 GHz), the information is limited resulting in inadequate representation of all conditions. These channel selections work for warm waters, but they all show weak performance in cold and rough waters for the RE algorithm. A good performance should not only be judged on the overall performance, since it depends on the number of matchups representing the given conditions, but it should also consider the spread in performance between the different observing conditions.

The overall improvement in SST performance (i.e. decrease in rstd when compared to drifter SST) of including the different frequencies (V and H polarization) can be seen in the first two columns of.

Table 3. These are based on the difference in performance between the algorithm that includes the frequency considered and the same channel configuration excluding the frequency considered. The improvements by adding the 6 GHz channels are thus based on the comparison of the 10, 18, 23, 36 GHz against the AMSR-E configuration, while the statistics on each of the other channels are based on a comparison of 7 pairs of channel configurations (all including the 6 GHz channels). The channels with the largest impact have been marked as bold in the table. The table shows that the OE and the RE algorithm agree that (not surprisingly) the most important channels for SST retrievals are the 6 GHz channels, followed by the 10 and 18 GHz

channels.

Fig. 7 shows the sensitivity (Eq. (3)) to SST obtained using the OE algorithm for the different channel configurations during the different weather and surface conditions. The sensitivities to SST are generally high (mean value of 0.98) and the variations are small, but significant. Using 500 bootstrap samples with replacement (same size as N), the average width of the 90% confidence intervals is 2.44e-05 when considering the different weather/surface conditions and channel selections. The maximum width of the 90% confidence intervals is 8.77e-05 and calculated for the WS > 10 m s⁻¹ and the 6, 10 GHz channel data subset. The high sensitivities are explained by the increased uncertainty on first guess SST. As more channels are included the sensitivity increases (in particular for cold waters), with the 6, 10 GHz configuration having the lowest sensitivity. This should be viewed in context of the performance of the retrieved SST against in situ SST in Fig. 6a, where increased number of channels improves the performance over the range of different observing conditions. The lowest sensitivity is generally seen for cold SST and high wind speeds, which explains the poor OE performance in these conditions using all channel configurations (Fig. 6a).

The sensitivity to TCLW (not shown) is likewise very high (mean value of 1.00) across the 15 channel selections, due to relative high uncertainty on ERA-I TCLW, which means that the retrieved TCLW is independent of the first guess from ERA-I. The sensitivity to WS and TCWV (also not shown) vary across the different channel selections depending on the information available in the selected channels, with the mean values of 0.93 and 0.44, respectively. The increase in sensitivities with inclusion of different frequencies (V and H polarization) can be seen in the last four columns of.

Table 3. The addition of the 36 GHz channels shows the largest increase in both the WS and TCLW sensitivity, followed by the 18, 23 and 10 GHz channels, while the 6 GHz channels give the smallest increase in sensitivity. For the TCWV sensitivity, the 23 GHz channels show the largest increase, followed by the 36 and 18 GHz channels and with limited impact from the 6 and 10 GHz channels. For the SST sensitivity, the 6 GHz channels show the largest increase, and leave the remaining channels with a small impact on the sensitivity in comparison.

4.2. Geographical dependencies for selected channel configurations

Fig. 8 shows the global performance of retrieved SST when compared

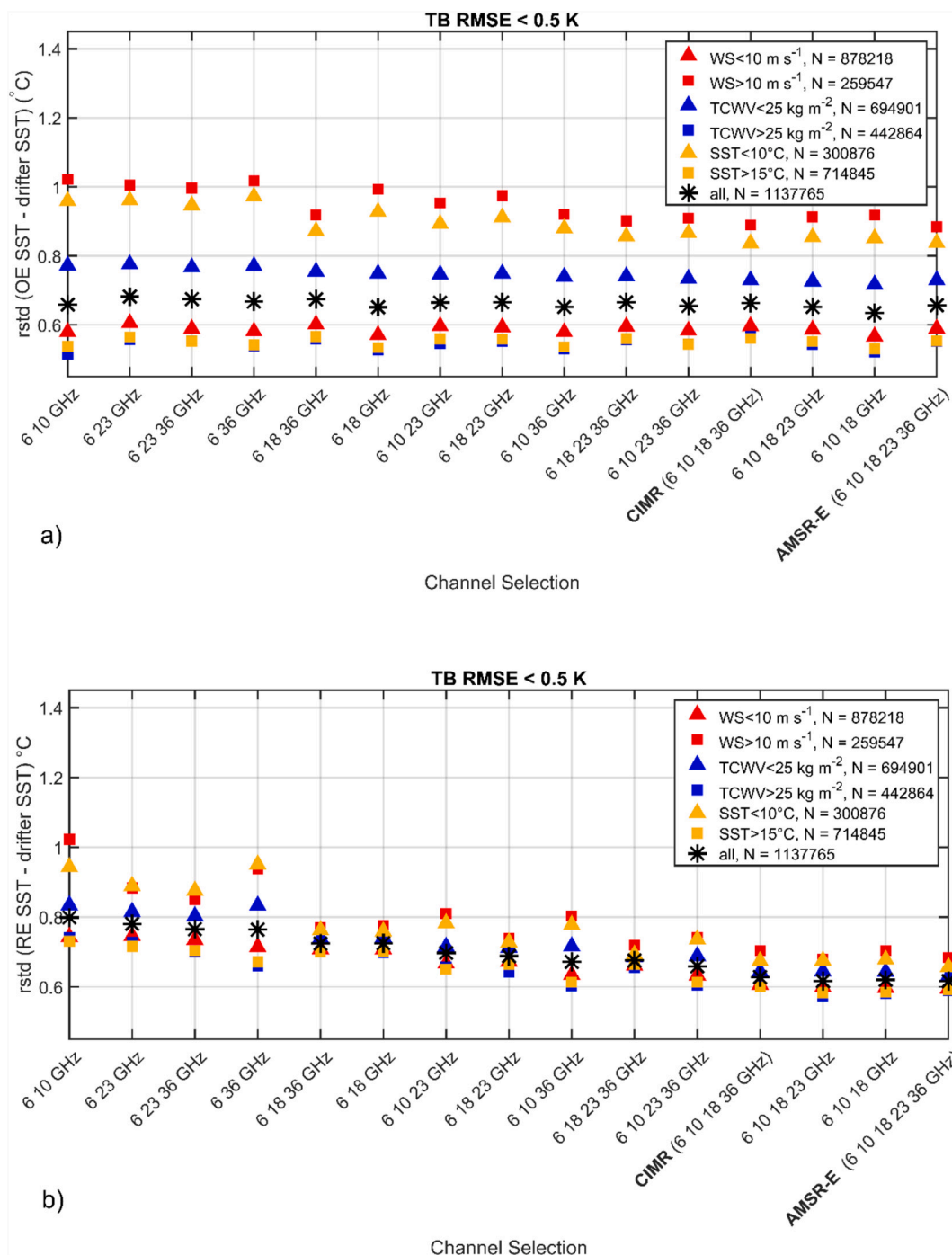


Fig. 6. Robust standard deviation of retrieved SST against drifter SST for different conditions and channel selections using a) the OE algorithm and b) the RE algorithm. The F2 (TB RMSE<0.5 K) filter has been applied for both the OE and RE algorithm and N is the number of matchups in each subset. The channel configurations are ordered from the highest to the lowest standard deviations using “all” conditions/matchups after F1 filtering (TB RMSE<0.25 K) for the RE algorithm.

to drifters for the RE and OE algorithms, respectively, for the AMSR-E channel configuration using the F3 filter. In general, the best performance is seen for low latitudes, while the high latitude and high variability regions show increased standard deviations. This is consistent with the fact that $\partial TB / \partial SST$ is smaller for cold waters compared to warm waters, as is also shown in Fig. 2a. Sea ice and a much smaller Rossby radius (compared to low latitudes), resulting in much smaller scale of eddies and fronts, further complicate SST retrievals in high latitudes. Better spatial resolution (as expected by CIMR) will make it easier to detect these features and therefore improve high latitude retrievals. The large standard deviations in the Sea of Japan are evident for all channel

combinations and both types of retrieval algorithms, and are likely effects from RFI at 6 GHz and RFI at 10 and/or 18 GHz, which are not removed by the applied RFI filters (see Section 2.1). Larger standard deviations are seen both with and without the 6 GHz channels, indicating that some matchups are contaminated at 6 GHz, while others are contaminated at 10 GHz and/or 18 GHz. Therefore, more sophisticated RFI filtering may be required, such as being planned for on-board implementation on CIMR. Since, the effect is seen in all channel selections it will not change the conclusions drawn in this study. The OE algorithm shows larger latitudinal differences in performance, with a better performance than the RE algorithm in the region between 25 N

Table 3

Improvements in SST retrievals compared to drifters for the OE and RE algorithms (column 1–2), and the increase in sensitivities (column 3–6), by including information from individual frequencies (both V and H polarization) using the F2 (TB RMSE < 0.5 K) filter. The largest increases in SST performances and sensitivities have been marked with bold.

	OE SST	RE SST	$\Delta A_{1,1}$	$\Delta A_{2,2}$	$\Delta A_{3,3}$	$\Delta A_{4,4}$
			(WS)	(TCWV)	(TCLW)	(SST)
6 GHz	0.2402	0.0907	0.0210	0.0140	0.0000	0.0145
10 GHz	0.0876	0.0148	0.0372	0.0913	0.0002	0.0013
18 GHz	0.0811	0.0117	0.0431	0.2762	0.0017	0.0007
23 GHz	0.0309	0.0089	0.0339	0.5984	0.0011	0.0007
36 GHz	0.0289	0.0114	0.0950	0.4939	0.0039	0.0011

and 25 S, but a decrease in the performance at latitudes above 40°. The smaller latitudinal dependence in the RE algorithm indicates that the statistical model finds a way to compensate for the reduced sensitivity in colder waters using information from the other channels and the covariances between the geophysical parameters that have an impact on the observed brightness temperatures.

Fig. 9 shows how the performance of the three channel selections: 6, 10, 18 GHz, 6, 10, 23 GHz, and CIMR differs from the performance using the AMSR-E channel configuration for the OE and RE algorithm, respectively. Using the 6, 10, 18 GHz channels improves the performance in the equatorial region (and mid-latitudes for the OE algorithm) compared to the AMSR-E configuration. However, in the high latitudes (and further into the mid-latitudes for the RE algorithm) the AMSR-E configuration outperforms the 6, 10, 18 GHz configuration. The

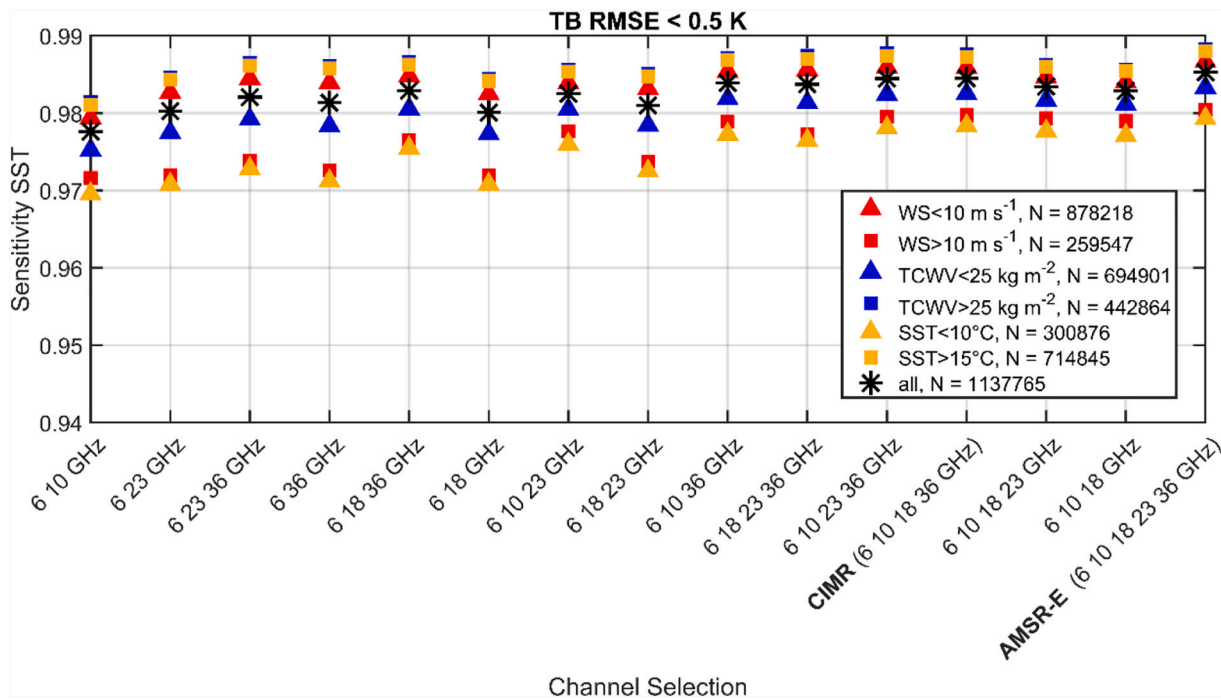


Fig. 7. The sensitivity to SST for the different channel selections and different weather/surface conditions using the same ranking order as in the previous figures and the F2 (TB RMSE < 0.5 K) filtering. N is the number of matchups in each subset.

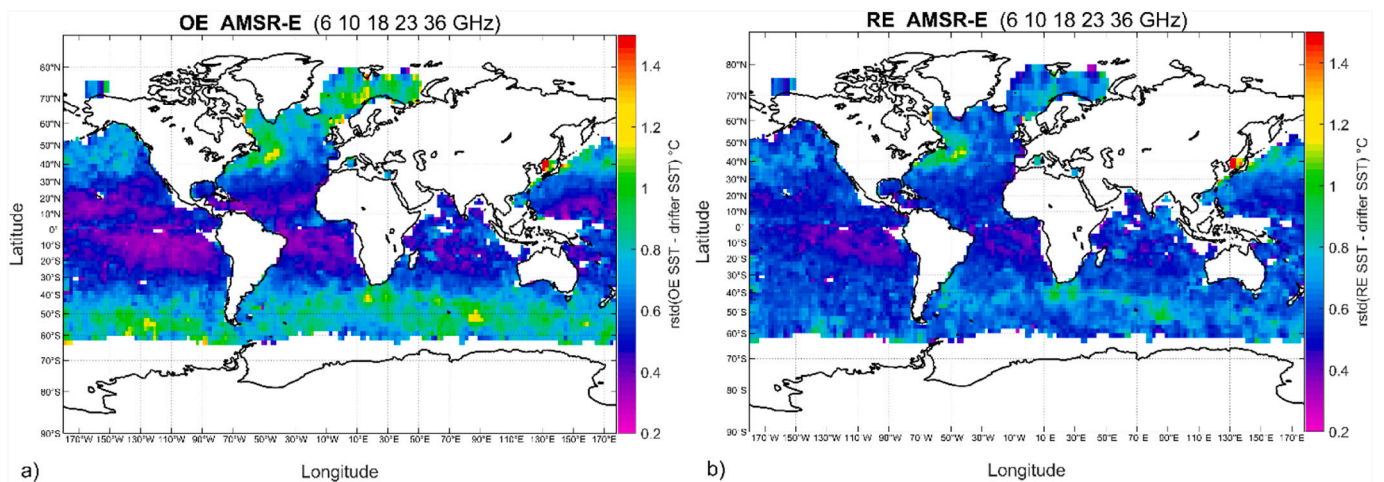


Fig. 8. Retrieved SST performance (robust standard deviations, rstd) against drifter SST using the AMSR-E (6, 10, 18, 23, 36 GHz) channel selection for a) the OE algorithm and b) the RE algorithm, using the F3 (3RSTD) filter. The geographical statistics have been gridded using a grid size of 5 degrees, with a minimum of 50 matchups per grid cell.

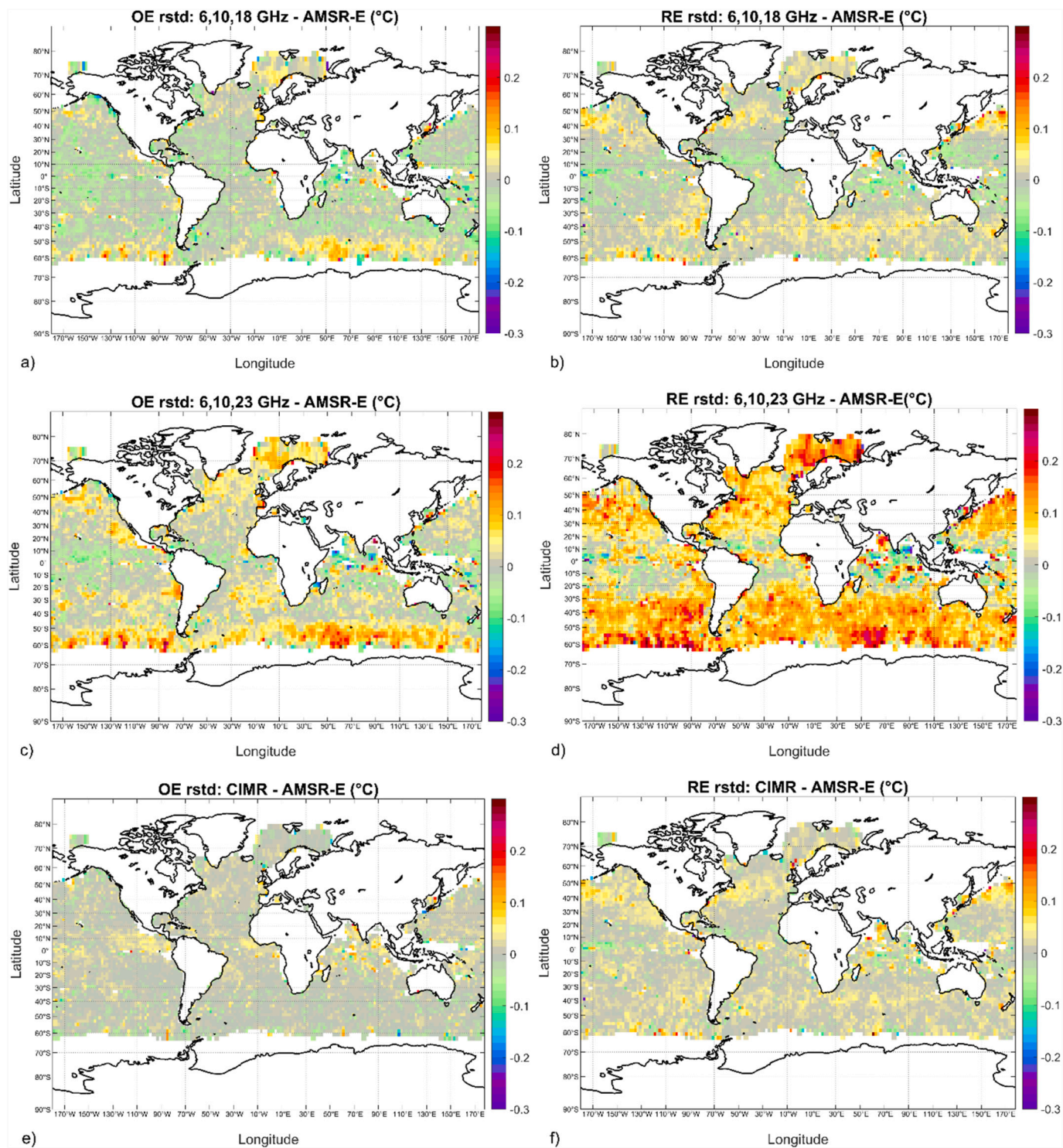


Fig. 9. Difference in robust standard deviations (retrieved minus drifter SST) (rstd) between channel configurations 6, 10, 18 GHz and the AMSR-E channel configuration using a) the OE algorithm, and b) the RE algorithm. Similar, the differences in rstd between 6, 10, 23 GHz and AMSR-E are shown for the OE (c) and RE (d) algorithms and the differences in rstd between CIMR and AMSR-E for the OE (e) and RE (f) algorithms. The F3 (3RSTD) filter has been used in all figures. The geographical statistics have been gridded using a grid size of 5 degrees, with a minimum of 50 matchups per grid cell.

largest reductions in performance (compared to AMSR-E) are seen in the comparison of the 6, 10, 23 GHz configuration for both algorithms, with the most pronounced degradation for the RE algorithm. For both algorithms, the degradations are concentrated in the high latitudes (and mid latitudes for the RE algorithm), while the 6, 10, 23 GHz configuration seems to perform slightly better in the equatorial region. Both the OE and RE algorithms show the best agreement between the CIMR and

AMSR-E channel selections, with the smallest differences using the OE algorithm. These findings have been summarized in Table 4 for the nine regions shown in Fig. 10.

Table 4 shows the performance of the four channel configurations using the OE and RE algorithms for each of the nine regions. For all channel selections, the best performance is seen in the equatorial region, with decreasing performance towards the poles. This latitudinal

Table 4

The retrieved versus drifter SST robust standard deviations (°C) within each region using the OE and RE algorithm, for each of the four channel selections using the F3 filter.

Region	RE algorithm				OE algorithm				
	6, 10, 18	6, 10, 23	CIMR	AMSR-E	6, 10, 18	6, 10, 23	CIMR	AMSR-E	N
Arctic	0.70	0.82	0.69	0.67	0.92	0.96	0.90	0.89	109,493
Subpolar North Atlantic	0.67	0.75	0.68	0.66	0.82	0.85	0.82	0.82	43,160
North Atlantic	0.62	0.68	0.63	0.62	0.57	0.60	0.59	0.59	110,870
North Pacific	0.64	0.71	0.65	0.63	0.58	0.62	0.60	0.60	163,072
Equatorial Region	0.53	0.57	0.55	0.55	0.44	0.44	0.48	0.47	188,331
South Atlantic	0.61	0.69	0.62	0.61	0.60	0.63	0.61	0.61	76,185
South Pacific	0.58	0.65	0.58	0.57	0.53	0.56	0.55	0.54	116,675
South Indian Ocean	0.63	0.70	0.63	0.61	0.63	0.65	0.65	0.65	83,632
Southern Ocean	0.68	0.79	0.67	0.65	0.83	0.87	0.82	0.83	174,069
All regions	0.62	0.70	0.63	0.62	0.63	0.66	0.66	0.66	1,065,487

Bold indicates the lowest robust standard deviation among the channel selections for each region and both algorithms. N is the number of matchups within each region.

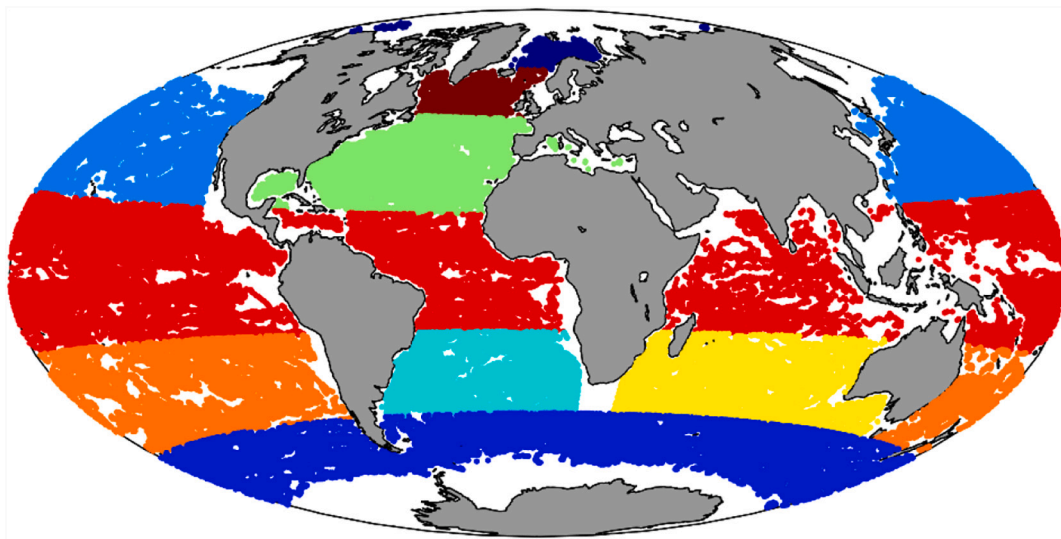


Fig. 10. The matchups in the nine selected regions for which the algorithms have been evaluated.

dependence is more pronounced for the OE algorithm compared to the RE algorithm, in all configurations. The 6, 10, 18 GHz combination shows very good performance in particular for the OE algorithm, where it outperforms the AMSR-E selection in most regions (except for the high latitudes). The AMSR-E and CIMR configurations show very similar performance in all regions.

Fig. 11 shows the seasonal cycle of the robust standard deviations of retrieved minus drifter SST for the same four channel selections using both retrieval algorithms in the nine different regions. The high latitudes show a clear seasonal cycle, with the lowest standard deviations during local summer (warm SST) for both algorithms. The high latitude regions also show the largest differences between the RE and OE performance, which is particularly true during local winter time, where the RE algorithm performs better than the OE algorithm. For most regions, the 6, 10, 23 GHz configuration gives the highest standard deviations for both retrieval algorithms. The RE algorithm shows very similar seasonal performance for the 6, 10, 18 GHz, CIMR and AMSR-E channel configurations for all regions. However, large differences between these configurations and the 6, 10, 23 GHz configuration are observed using the RE algorithm, especially at high latitudes during winter, where significant improvements are seen when replacing the 23 GHz with the 18 GHz channels.

5. Discussion

This study shows that the inclusion of more channels and more

information in the retrieval reduces the uncertainty in the SST retrievals. This is clearly seen for the RE algorithm, while the OE algorithm shows less variability in overall performance among the different channel selections. This difference can be explained by the fundamental difference in the two types of retrieval algorithms. The statistical retrieval is based solely on the information available in the selected satellite channel observations. Conversely, the OE types of retrieval algorithm use a priori information to constrain the retrievals. If limited information is available in a given set of channels, the sensitivity will decrease and as a result, the algorithm will put more weight on the first guess. The largest decreases in the wind speed (i.e. sea surface roughness) sensitivity are seen for retrievals in cases, where 36, 23 or 18 GHz are left out from the OE retrieval. Theoretically, the sensitivity to WS is largest at 10 and 18 GHz (Fig. 2b). In the approach used here however, the fact that individual channels are sensitive to other parameters is turned to an advantage by the simultaneous use of all channels. The largest decrease in water vapor sensitivity is seen for retrievals, where the 23 and 36 GHz observations are left out. In particular, the retrieved water vapor will in these cases be dominated by the first guess from ERA-I, which therefore will keep the OE retrievals close to the true state even with limited information from the brightness temperatures. This will be the case in a realistic scenario, as the one considered here, where WS and TCWV information is available from NWP at a similar quality as ERA-I to be used as first guess for the OE algorithm. The OE retrieval algorithm is thus more robust towards different channel combinations, compared to the statistical RE algorithm.

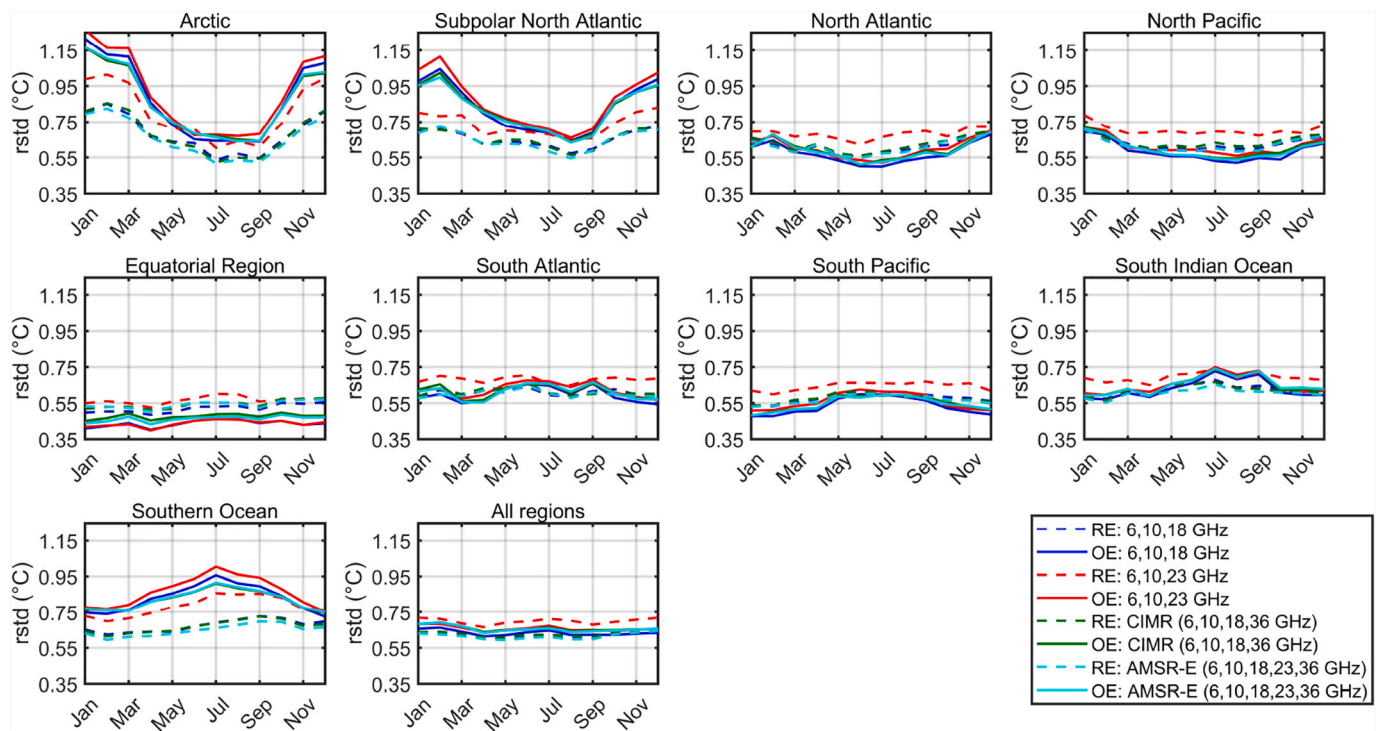


Fig. 11. Retrieved SST performance against drifters for the four different channel selections: 6, 10, 18 GHz, 6, 10, 23 GHz, 6, 10, 18, 36 GHz, and 6, 10, 18, 23, 36 GHz as a function month for the different regions using the F3 filter for both retrieval algorithms.

By including more channels both algorithms show a better representation over the range of the different observing conditions. The performance of the OE algorithm (and the different channel selections) is sensitive to the atmospheric and oceanic conditions with elevated uncertainties for cold and rough waters for all channel selections. The increased uncertainties in cold waters are related to the decreased sensitivity to SST for the low frequency channels (in particular at V polarization) as seen in Fig. 2a. Kilic et al. (2019) found that cold SSTs are a general source of disagreement between simulated and observed brightness temperatures in the emissivity models and they explained this in part by uncertainties in the modelling of the dielectric constants of sea water, but also by inaccuracy in the reanalysis data and high wind speed effects in colder areas. Fig. 2a shows that the sensitivity to SST in cold waters to a large extent originates from the higher frequency channels, with decreasing brightness temperatures for increasing SST. This suggest that the increased uncertainties for cold SST could also be attributed to uncertainty in modelling the higher frequencies due to e.g. imperfections in the atmospheric emissivity model. This effect could possibly to some extent be reduced by including the covariances (off-diagonals in S_a) between the geophysical parameters in the OE algorithm. However, these are currently not well known and it is a complete study to estimate them (see recommendations for future work in Section 6). Using the RE algorithm, the increased uncertainties for cold waters and strong surface roughness is most pronounced for the two-frequency configurations without 18 GHz, while more (>2) frequencies provide enough information to balance the lower sensitivity in cold and rough waters. This indicates that the statistical RE algorithm compensates for the reduced sensitivity of the low frequency channels in colder waters by using information from the higher frequency channels and possibly the covariances between the geophysical parameters influencing the observations. These results demonstrate the importance of using in situ observations and several types of SST retrievals to assess the relative performance of the different channel selections. Information content studies are typically performed using the OE type of algorithms, but different conclusions might be reached using other types of retrieval methods, as indicated here.

Both the OE and RE algorithms agree that in a three frequency selection, the 6, 10, 18 GHz combination is better than 6, 10, 23 GHz, considering the nine different regions in Table 4 and performance throughout the year (Fig. 11). In general, the results for the OE and RE algorithms consistently show that the CIMR channel selection performs very well compared to the AMSR-E configuration. It should be noted that the presented results do not correspond to the expected CIMR performance, as e.g. the CIMR NEDTs will be different from the AMSR-E NEDTs and the CIMR footprints will be significantly smaller than the AMSR-E footprints. Neglecting these observational characteristics for the CIMR instrument, means that the absolute performance of the CIMR retrievals is expected to be significantly better than shown here due to smaller NEDTs and smaller footprints, which better resolve spatial variability at the key frequencies. However, as we focus on the differences between the channel combinations, we consider the AMSR-E NEDTs suitable for the current study. Using the AMSR2 observations instead of AMSR-E observations would very likely resemble the results presented here, as it was shown in Alerskans et al. (2020) that the retrievals from the two instruments showed very similar performance and uncertainty characteristics.

The very good performance of the 6, 10 and 18 GHz combination shown here support the channel selection for the CIMR mission, as the CIMR requirement of the NEDT for the 36 GHz is elevated (Donlon, 2019) and therefore is likely to contribute with limited information to the SST retrievals. Also, note that the CIMR configuration referred to in this paper is without the 1.4 GHz channels (L-band). This could introduce a difference in the wind speed behavior, particularly for high wind speeds (Meissner et al., 2017; Reul et al., 2012, 2016, 2017), and also on the impact of salinity. However, for the winds considered here (<20 m s⁻¹) it was shown in Alerskans et al. (2020) that sufficient information was available in the AMSR-E observations to perform an accurate wind speed retrieval.

To obtain realistic retrieval estimates using the OE algorithm, an accurate forward model is needed to account for the brightness temperature dependencies to the relevant geophysical parameters. The forward model used is based on an earlier version of the RSS (Remote

Sensing Systems) model (Wentz and Meissner, 2000), which showed the least discrepancy with observations in Kilic et al. (2019). The improvements applied to the forward model (Nielsen-Englyst et al., 2018) results in even better agreement with observations and consequently good SST retrievals. The forward model sensitivities presented in this paper (see Fig. 2) indicate a close relationship with Prigent et al. (2013) and Kilic et al. (2018), whereas the use of RTTOV and FASTEM (FAST microwave Emissivity Model) in Pearson et al. (2018) shows significantly different emissivity/brightness temperature dependencies with respect to wind speed and sea surface salinity.

One of the strengths of the OE algorithm is that it offers several possibilities to obtain realistic error estimates and in fact it directly provides a theoretical error estimate for each retrieval. The theoretical uncertainties presented in Section 3.1.1 are in good agreement with those found in Prigent et al. (2013) and Kilic et al. (2018). A validation of the estimated theoretical uncertainties is shown in Fig. 12, where the OE versus drifter SST differences are displayed against the theoretical uncertainties obtained from Eq. 2. The dashed lines represent the ideal uncertainty under the assumptions that drifting buoys have a total uncertainty of 0.2 °C and that the mean global point to footprint sampling uncertainty is 0.15 °C, derived as in Alerskans et al. (2020) taking into account the footprint of the AMSR-E instrument. The figure shows reasonable agreement between the observed uncertainties and the theoretical uncertainties, which is computed for each retrieval in the OE algorithm, but also demonstrates that the theoretical retrieval uncertainties are not representing the true uncertainties for all conditions, demonstrating the need for use of in situ observations for this type of assessment.

6. Future work

This study shows that the statistical retrieval algorithm is more robust over the range of observing conditions, when compared with the physically based OE algorithm that can include information from first guess fields. Future work should therefore aim at improving the OE algorithm. This can be done in several ways. One way is to improve the OE statistics for PMW observations e.g. by including the error covariances for the geophysical variables in the retrieval. The error covariances for the geophysical variables influencing passive microwave observations are currently not well known and it is a complete study to estimate these. One recent study has been conducted to estimate error covariance

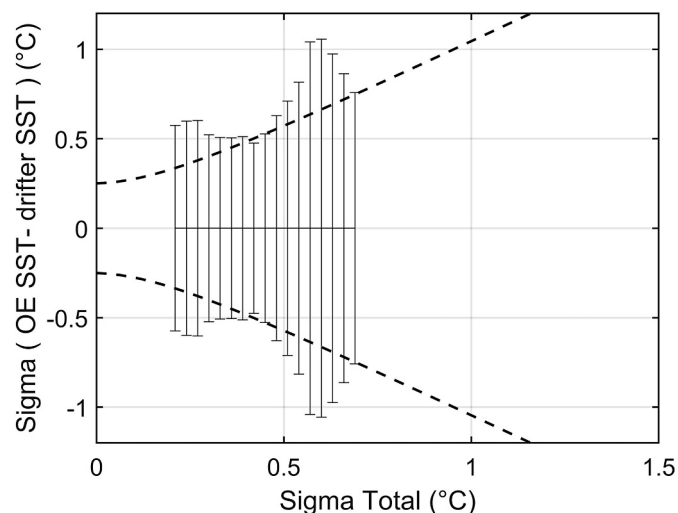


Fig. 12. Theoretical uncertainty validation with respect to drifter SST for the OE algorithm. Dashed lines show the ideal uncertainty model accounting for uncertainties in drifter SST and the sampling error. Solid black lines show one standard deviation of the retrieved minus drifter differences for each 0.03 °C bin.

parameters (and a bias correction) using IR observations (Merchant et al., 2020) and it looks very promising. Repeating the work done by Merchant et al. (2020) should be the focus of future work to improve the OE algorithm. Another way to improve the OE algorithm is to update the forward model to more accurately model the emissivity over the given frequency range and accounting for the different observing conditions. As also recognized in Kilic et al. (2019), current ocean emissivity models have issues particularly in cold and rough waters, and future efforts should thus be devoted to address these issues. The addition of the 1.4 GHz channels in the retrieval to prepare for the CIMR observations is another interesting task that would add information about the salinity and high wind speeds to the channel combinations considered here. Note, however, that the spatial resolution of the 1.4 GHz channels on the CIMR will be significantly coarser than e.g. the 6 GHz observations, which adds a complication to the use of the 1.4 GHz channels.

Both retrieval algorithms agree that the 6, 10, 18 GHz is better than the 6, 10, 23 GHz combination. Although the 23 GHz should be considered the best channel to account for uncertainties due to water vapor variability, these results show that it might add more noise being in the absorption band, while the 18 GHz channels are able to correct for the relative small uncertainties in the 6 GHz channels due to water vapor variability. If 10 GHz is used as the primary frequency for SST retrievals, the 23 GHz may be needed as the 10 GHz channels are affected more by water vapor than the 6 GHz channels. Future studies could extend this study to investigate other channel combinations, including those omitting the lowest frequency(ies) in order to obtain better spatial resolution.

Additional future tasks could also be to examine the impact on the results shown here by using a different forward model or by using ERA5 (Copernicus Climate Change Service (C3S), 2017) instead of ERA-I reanalysis data for training the RE algorithm and for first guess in the OE algorithm, respectively. Irrespective of the different improvements made to the retrievals and the forward models, this study demonstrates the importance of comparing different types of retrieval algorithms (physical versus statistical) using in situ observations before determining the best suitable SST retrieval for a new instrument, such as CIMR.

7. Conclusion

The aim of this study is to analyze the impact of using different channel selections on retrieved sea surface temperature (SST) and to assess the performance of two different types of retrieval algorithms. The first algorithm is a physically based optimal estimation (OE) algorithm (Nielsen-Englyst et al., 2018), which inverts a forward model to retrieve SST, wind speed (WS), total column water vapor (TCWV) and total cloud liquid water (TCLW), while the second algorithm is a statistical regression (RE) based algorithm, which retrieves WS and SST (Alerskans et al., 2020). Here, we use AMSR-E brightness temperatures from 2010 to retrieve SST using different channel combinations in both algorithms, which are then compared to independent in situ SSTs.

This study demonstrated similarities with Kilic et al. (2018) using the OE algorithm, but it also demonstrated the importance of using two different types of retrieval algorithms. Information content studies are typically performed using the OE type of algorithms, and the current forward models have issues reproducing observations in cold waters (Kilic et al., 2019). Conversely, statistical retrievals, such as the RE algorithm, are the often used for generating operational and climate data records of PMW SST. The RE algorithm used here is able to compensate for the decreased sensitivity for cold SSTs, due to the nature of the statistical algorithm. This study also highlights the importance of assessing the retrievals against real reference observations, to ensure that all the different uncertainties contributions are included when drawing conclusions on the impact of using different channels for SST retrievals.

Both algorithms show (as expected) an increase in performance when more channels are included in the retrieval, since more channels

allow a better representation of the different observing conditions (e.g. cold waters). Both algorithms agree that the 6, 10, 18 GHz channel configuration is better than 6, 10, 23 GHz for SST retrievals. Furthermore, it is evident that withholding observations from the 23 and 36 GHz channels from the retrieval has the least impact on the SST performance. The proposed CIMR constellation (not considering the 1.4 GHz channels) has proven to perform very well when compared to an AMSR-E like constellation (excluding the 89 GHz channels) using both the OE and RE algorithm. The actual CIMR performance is expected to be significantly better than shown here due to smaller NEDTs and footprints. The proposed CIMR constellation includes observations at 1.4 GHz (L-band), which will further add information to both SST and WS retrievals (Reul et al., 2012, 2017), but with decreased spatial resolution and with larger influence from sea surface salinity and the ionosphere (i.e. Faraday rotation).

The comparison of the two retrieval algorithms demonstrates strengths and weaknesses related to their use. One of the strengths of the RE algorithm is its ability to compensate for the decreased sensitivity to SST in cold waters as mentioned above. The OE algorithm, on the other hand, shows very good capability during conditions with fewer channels. This can become very useful e.g. in case of instrument failure and we believe that this capability will be useful to develop alternative plan for emergency status of the instrument. Another advantage of the OE algorithm is, that it can be used to retrieve SST from day 1 for all channel combinations, while the RE algorithm requires significant number of matchups for training each combination of channels before it can be used for retrievals. This is important to consider for potential day 1 SST

products from e.g. CIMR. All of above needs to be considered before an algorithm is selected for a given application and multiple utilization of the two algorithms is definitely an advantage.

Overall, new insights have been gained into the performance of the SST retrievals for different channel combinations. This is important for designing and evaluating new satellite configurations or for assessing the impact of existing satellite observations in the case of failing channels or RFI contaminated retrievals.

Declaration of Competing Interest

The authors declare that they have no known competing financial interests or personal relationships that could have appeared to influence the work reported in this paper.

Acknowledgements

The two SST retrieval algorithms have been developed within the ESA-CCI SST project and this analysis has been carried out as a part of the ESA CIMR contract no. 4000125255/18/NL/AI. ICOADS data are available at <https://icoads.noaa.gov/>. EN4 version 4.2.0 is available at <https://www.metoffice.gov.uk/hadobs/en4/>. The resampled L2A data product AMSR-E V12 is produced by Remote Sensing Systems (RSS) and distributed by NASA's National Snow and Ice Data Center (NSIDC). Data are available at https://nsidc.org/data/ae_l2a. The ERA-Interim reanalysis data is available at <https://www.ecmwf.int/en/forecasts/dataset/reanalysis-datasets/era-interim>.

Appendix A. Appendix

	0.094	0.106	0.023	-0.042	-0.002	-0.119	0.092	0.002	0.081	-0.008
	0.106	0.302	-0.067	-0.105	-0.075	-0.220	0.129	0.039	0.135	0.006
	0.023	-0.067	0.127	0.048	0.113	-0.011	0.092	-0.071	0.084	-0.059
	-0.042	-0.105	0.048	0.090	0.026	0.047	0.005	-0.025	0.000	-0.028
S_e	-0.002	-0.075	0.113	0.026	0.243	0.073	0.101	-0.148	0.132	-0.107
	-0.119	-0.220	-0.011	0.047	0.073	0.275	-0.154	-0.052	-0.130	-0.011
	0.092	0.129	0.092	0.005	0.101	-0.154	0.271	-0.101	0.231	-0.089
	0.002	0.039	-0.071	-0.025	-0.148	-0.052	-0.101	0.118	-0.101	0.076
	0.081	0.135	0.084	0.000	0.132	-0.130	0.231	-0.101	0.286	-0.120
	-0.008	0.006	-0.059	-0.028	-0.107	-0.011	-0.089	0.076	-0.120	0.076

References

Alerskans, E., Høyer, J.L., Gentemann, C.L., Pedersen, L.T., Nielsen-Englyst, P., Donlon, C., 2020. Construction of a climate data record of sea surface temperature from passive microwave measurements. *Remote Sens. Environ.* 236, 111485. <https://doi.org/10.1016/j.rse.2019.111485>.

Ashcroft, P., Wentz, F.J., 2013. AMSR-E/Aqua L2A Global Swath Spatially-Resampled Brightness Temperatures (Tb), Version 3. https://doi.org/10.5067/AMSR-E/AE_L2A.003.

Bidwell, S.W., Flaming, G.M., Durning, J.F., Smith, E.A., 2005. The global precipitation measurement (GPM) microwave imager (GMI) instrument: role, performance, and status. In: *Proceedings. 2005 IEEE International Geoscience and Remote Sensing Symposium, 2005. IGARSS '05., 1 IEEE, Seoul, Korea*, pp. 83–86.

Braakmann-Folmann, A., Donlon, C., 2019. Estimating snow depth on Arctic Sea ice using satellite microwave radiometry and a neural network. *Cryosphere* 13 (9), 2421–2438. <https://doi.org/10.5194/tc-13-2421-2019>.

Brasnett, B., Colan, D.S., 2016. Assimilating retrievals of sea surface temperature from VIIRS and AMSR2. *J. Atmos. Ocean. Technol.* 33 (2), 361–375. <https://doi.org/10.1175/JTECH-D-15-0093.1>.

Chang, P.S., Jelenak, Z., Alswelss, S., 2015. Algorithm Theoretical Basis Document: GCOM-W1/AMSR2 Day-1 EDR version 1.0 [online] Available from: https://www.star.nesdis.noaa.gov/jps/documents/ATBD/ATBD_AMSR2_Ocean_EDR_v2.0.pdf.

Chelton, D.B., Freilich, M.H., 2005. Scatterometer-based assessment of 10-m wind analyses from the operational ECMWF and NCEP numerical weather prediction models. *Mon. Weather Rev.* 133 (2), 409–429. <https://doi.org/10.1175/MWR-2861.1>.

Chelton, D.B., Wentz, F.J., 2005. Global microwave satellite observations of sea surface temperature for numerical weather prediction and climate research. *Bull. Am. Meteorol. Soc.* 86 (8), 1097–1115. <https://doi.org/10.1175/BAMS-86-8-1097>.

Ciani, D., Santoleri, R., Liberti, G.L., Prigent, C., Donlon, C., Buongiorno Nardelli, B., 2019. Copernicus imaging microwave radiometer (CIMR) benefits for the Copernicus level 4 sea-surface salinity processing chain. *Remote Sens.* 11 (15), 1818. <https://doi.org/10.3390/rs11151818>.

Copernicus Climate Change Service (C3S), 2017. ERA5: Fifth Generation of ECMWF Atmospheric Reanalyses of the Global Climate. Copernicus Climate Change Service Climate Data Store (CDS) [online] Available from: <https://cds.climate.copernicus.eu/cdsapp#!/home> (Accessed 9 May 2019).

Dee, D.P., Uppala, S.M., Simmons, A.J., Berrisford, P., Poli, P., Kobayashi, S., Andrae, U., Balmaseda, M.A., Balsamo, G., Bauer, P., Bechtold, P., Beljaars, A.C.M., van de Berg, L., Bidlot, J., Bormann, N., Delsol, C., Dragani, R., Fuentes, M., Geer, A.J., Haimberger, L., Healy, S.B., Hersbach, H., Hólm, E.V., Isaksen, I., Kållberg, P., Köhler, M., Matricardi, M., McNally, A.P., Monge-Sanz, B.M., Morcrette, J.J., Park, B.K., Peubey, C., de Rosnay, P., Tavolato, C., Thépaut, J.N., Vitart, F., 2011. The ERA-Interim reanalysis: Configuration and performance of the data assimilation system. *Q. J. R. Meteorol. Soc.* 137 (656), 553–597. <https://doi.org/10.1002/qj.828>.

Donlon, C., Rayner, N., Robinson, I., Poulter, D.J.S., Casey, K.S., Vazquez-Cuevo, J., Armstrong, E., Bingham, A., Arino, O., Gentemann, C., May, D., LeBorgne, P., Piollé, J., Barton, I., Beggs, H., Merchant, C.J., Heinz, S., Harris, A., Wick, G., Emery, B., Minnett, P., Evans, R., Llewellyn-Jones, D., Mutlow, C., Reynolds, R.W., Kawamura, H., 2007. The global ocean data assimilation experiment high-resolution sea surface temperature pilot project. *Bull. Am. Meteorol. Soc.* 88 (8), 1197–1213. <https://doi.org/10.1175/BAMS-88-8-1197>.

Donlon, C., Casey, K.S., Gentemann, C., Harris, A., 2010. Successes and challenges for the modern sea surface temperature observing system. In: Hall, J., Harrison, D.E., Stammer, D. (Eds.), *Proceeding of OceanObs'09: Sustained Ocean Observations and Information for Society, 2. ESA Publication WPP-306, Venice Italy, 21–25 September 2009*.

Donlon, C. J.: Copernicus Imaging Microwave Radiometer (CIMR) Mission Requirements Document. Version 3.0., [online] Available from: <https://cimr.eu/sites/cimr.met>.

- no/files/documents/CIMR-MRD-v3.0-20190930-Issued.pdf (Accessed 9 January 2020), 2019.
- Draper, D.W., Newell, D.A., Wentz, F.J., Krimchansky, S., Skofronick-Jackson, G.M., 2015. The global precipitation measurement (GPM) microwave imager (GMI): instrument overview and early on-orbit performance. *IEEE J. Sel. Top. Appl. Earth Observ. Remote Sens.* 8 (7), 3452–3462. <https://doi.org/10.1109/JSTARS.2015.2403303>.
- Embury, O., Merchant, C.J., Corlett, G.K., 2012. A reprocessing for climate of sea surface temperature from the along-track scanning radiometers: initial validation, accounting for skin and diurnal variability effects. *Remote Sens. Environ.* 116, 62–78. <https://doi.org/10.1016/j.rse.2011.02.028>.
- Fore, A.G., Yueh, S.H., Tang, W., Stiles, B.W., Hayashi, A.K., 2016. Combined active/passive retrievals of ocean vector wind and sea surface salinity with SMAP. *IEEE Trans. Geosci. Remote Sens.* 54 (12), 7396–7404. <https://doi.org/10.1109/TGRS.2016.2601486>.
- Gentemann, C.L., 2014. Three way validation of MODIS and AMSR-E Sea surface temperatures. *J. Geophys. Res. Oceans* 119 (4), 2583–2598. <https://doi.org/10.1002/2013JC009716>.
- Gentemann, C.L., Hilburn, K.A., 2015. In situ validation of sea surface temperatures from the GCOM-W1 AMSR2 RSS calibrated brightness temperatures: validation of RSS GCOM-W1 SST. *J. Geophys. Res. Oceans* 120 (5), 3567–3585. <https://doi.org/10.1002/2014JC010574>.
- Gentemann, C.L., Donlon, C.J., Stuart-Menteth, A., Wentz, F.J., 2003. Diurnal signals in satellite sea surface temperature measurements. *Geophys. Res. Lett.* 30 (3) <https://doi.org/10.1029/2002GL016291>.
- Gentemann, C.L., Meissner, T., Wentz, F.J., 2010. Accuracy of Satellite Sea surface temperatures at 7 and 11 GHz. *IEEE Trans. Geosci. Remote Sens.* 48 (3), 1009–1018. <https://doi.org/10.1109/TGRS.2009.2030322>.
- Gladkova, I., Ignatov, A., Shahriar, F., Kihai, Y., Hillger, D., Petrenko, B., 2016. Improved VIIRS and MODIS SST imagery. *Remote Sens. Environ.* 188, 1–10. <https://doi.org/10.1016/j.rse.2016.07.019>.
- Good, S.A., Martin, M.J., Rayner, N.A., 2013. EN4: quality controlled ocean temperature and salinity profiles and monthly objective analyses with uncertainty estimates: THE EN4 DATA SET. *J. Geophys. Res. Oceans* 118 (12), 6704–6716. <https://doi.org/10.1002/2013JC009067>.
- Hirabayashi, T., 2020. Contribution of JAXA's Earth Observation Missions to Water Cycle and Climate Studies, Disaster Mitigation, and Operational Applications, EGU General Assembly 2020, Online, 4–8 May 2020, EGU2020–19165. <https://doi.org/10.5194/egusphere-egu2020-19165>.
- Hollinger, J., 1971. Passive microwave measurements of sea surface roughness. *IEEE Trans. Geosci. Electron.* 9 (3), 165–169. <https://doi.org/10.1109/TGE.1971.271489>.
- Imaoka, K., Kachi, M., Kasahara, M., Ito, N., Nakagawa, K., Oki, T., 2010. Instrument performance and calibration of AMSR-E and AMSR2, international archives of the photogrammetry. *Remote Sens. Spat. Inform. Sci.* 38 (8), 13–18.
- Jakobson, E., Vihma, T., Palo, T., Jakobson, L., Keernik, H., Jaagus, J., 2012. Validation of Atmospheric Reanalyses over the Central Arctic Ocean: tara reanalyses validation. *Geophys. Res. Lett.* 39 (10) <https://doi.org/10.1029/2012GL051591>. N/a-N/a.
- Jiang, J.H., Su, H., Zhai, C., Perun, V.S., Del Genio, A., Nazarenko, L.S., Donner, L.J., Horowitz, L., Seman, C., Cole, J., Gettelman, A., Ringer, M.A., Rotstayn, L., Jeffrey, S., Wu, T., Briant, F., Dufresne, J.-L., Kawai, H., Koshiro, T., Watanabe, M., LÉcuyer, T.S., Volodin, E.M., Iversen, T., Drange, H., Mesquita, M.D.S., Read, W.G., Waters, J.W., Tian, B., Teixeira, J., Stephens, G.L., 2012. Evaluation of cloud and water vapor simulations in CMIP5 climate models using NASA "A-Train" satellite observations: EVALUATION OF IPCC AR5 MODEL SIMULATIONS. *J. Geophys. Res.-Atmos.* 117 (D14) <https://doi.org/10.1029/2011JD017237>.
- Kawanishi, T., Sezai, T., Ito, Y., Imaoka, K., Takeshima, T., Ishido, Y., Shibata, A., Miura, M., Inahata, H., Spencer, R.W., 2003. The advanced microwave scanning radiometer for the earth observing system (AMSR-E), NASDA's contribution to the EOS for global energy and water cycle studies. *IEEE Trans. Geosci. Remote Sens.* 41 (2), 184–194. <https://doi.org/10.1109/TGRS.2002.808331>.
- Kerr, Y.H., Waldteufel, P., Wigneron, J.-P., Delwart, S., Cabot, F., Boutin, J., Escorihuela, M.-J., Font, J., Reul, N., Gruhier, C., Juglea, S.E., Drinkwater, M.R., Hahne, A., Martín-Neira, M., Mecklenburg, S., 2010. The SMOS Mission: new tool for monitoring key elements of the global water cycle. *Proc. IEEE* 98 (5), 666–687. <https://doi.org/10.1109/JPROC.2010.2043032>.
- Kilic, L., Prigent, C., Aires, F., Boutin, J., Heygster, G., Tonboe, R.T., Roquet, H., Jimenez, C., Donlon, C., 2018. Expected performances of the Copernicus imaging microwave radiometer (CIMR) for an all-weather and high spatial resolution estimation of ocean and sea ice parameters. *J. Geophys. Res. Oceans* 123 (10), 7564–7580. <https://doi.org/10.1029/2018JC014408>.
- Kilic, L., Prigent, C., Boutin, J., Meissner, T., English, S., Yueh, S., 2019. Comparisons of ocean radiative transfer models with SMAP and AMSR2 observations. *J. Geophys. Res. Oceans* 124 (11), 7683–7699. <https://doi.org/10.1029/2019JC015493>.
- Kummerow, C., Barnes, W., Kozu, T., Shiue, J., Simpson, J., 1998. The tropical rainfall measuring mission (TRMM) sensor package. *J. Atmos. Ocean. Technol.* 15, 809–817.
- Le Traon, P.Y., Antoine, D., Bentamy, A., Bonekamp, H., Breivik, L.A., Chapron, B., Corlett, G., Dibarboure, G., Digiacomio, P., Donlon, C.J., Faugère, Y., Font, J., Girard-Ardhuin, F., Gohin, F., Johannessen, J.A., Kamachi, M., Lagerloef, G., Lambin, J., Larnicol, G., Le Borgne, P., Leuliette, E., Lindstrom, E., Martin, M.J., Maturi, E., Miller, L., Mingsen, L., Morrow, R., Reul, N., Rio, M.H., Roquet, H., Santoleri, R., Wilkin, J., 2015. Use of satellite observations for operational oceanography: recent achievements and future prospects. *J. Operat. Oceanogr.* 8 (sup 1), 12–27. <https://doi.org/10.1080/1755876X.2015.1022050>.
- Li, J.-L.F., Waliser, D., Woods, C., Teixeira, J., Bacmeister, J., Chern, J., Shen, B.-W., Tompkins, A., Tao, W.-K., Köhler, M., 2008. Comparisons of satellites liquid water estimates to ECMWF and GMAO analyses, 20th century IPCC AR4 climate simulations, and GCM simulations. *Geophys. Res. Lett.* 35 (19) <https://doi.org/10.1029/2008GL035427>.
- Liang, X., Yang, Q., Neger, L., Losa, S.N., Zhao, B., Zheng, F., Zhang, L., Wu, L., 2017. Assimilating Copernicus SST data into a pan-Arctic Ice-Ocean coupled model with a local SEIK filter. *J. Atmos. Ocean. Technol.* 34 (9), 1985–1999. <https://doi.org/10.1175/JTECH-D-16-0166.1>.
- Lipes, R.G., 1982. Description of SEASAT radiometer status and results. *J. Geophys. Res.* 87 (C5), 3385. <https://doi.org/10.1029/JC087C05p03385>.
- Meissner, T., Wentz, F., 2002. An updated analysis of the ocean surface wind direction signal in passive microwave brightness temperatures. *IEEE Trans. Geosci. Remote Sens.* 40 (6), 1230–1240. <https://doi.org/10.1109/TGRS.2002.800231>.
- Meissner, T., Wentz, F.J., 2012. The emissivity of the ocean surface between 6 and 90 GHz over a large range of wind speeds and earth incidence angles. *IEEE Trans. Geosci. Remote Sens.* 50 (8), 3004–3026. <https://doi.org/10.1109/TGRS.2011.2179662>.
- Meissner, T., Ricciardulli, L., Wentz, F.J., 2017. Capability of the SMAP Mission to measure ocean surface winds in storms. *Bull. Am. Meteor. Soc.* 98 (8), 1660–1677. <https://doi.org/10.1175/BAMS-D-16-0052.1>.
- Merchant, C.J., Harris, A.R., Murray, M.J., Zavody, A.M., 1999. Toward the elimination of bias in satellite retrievals of skin sea surface temperature 1. Theory, modeling and inter-algorithm comparison. *J. Geophys. Res. Oceans* 104 (C10), 23565–23578. <https://doi.org/10.1029/1999JC900105>.
- Merchant, C.J., Embury, O., Le Borgne, P., Belloc, B., 2006. Saharan dust in night-time thermal imagery: detection and reduction of related biases in retrieved sea surface temperature. *Remote Sens. Environ.* 104, 15–30.
- Merchant, C.J., Embury, O., Roberts-Jones, J., Fiedler, E., Bulgina, C.E., Corlett, G.K., Good, S., McLaren, A., Rayner, N., Morak-Bozzo, S., Donlon, C., 2014. Sea surface temperature datasets for climate applications from phase 1 of the European Space Agency climate change initiative (SST CCI). *Geosci. Data J.* 1 (2), 179–191. <https://doi.org/10.1002/gdj3.20>.
- Merchant, C.J., Embury, O., Bulgina, C.E., Block, T., Corlett, G.K., Fiedler, E., Good, S.A., Mittaz, J., Rayner, N.A., Berry, D., Eastwood, S., Taylor, M., Tsushima, Y., Waterfall, A., Wilson, R., Donlon, C., 2019. Satellite-based time-series of sea-surface temperature since 1981 for climate applications. *Sci. Data* 6 (1), 223. <https://doi.org/10.1038/s41597-019-0236-x>.
- Merchant, C.J., Saux-Picart, S., Waller, J., 2020. Bias correction and covariance parameters for optimal estimation by exploiting matched in-situ references. *Remote Sens. Environ.* 237, 111590. <https://doi.org/10.1016/j.rse.2019.111590>.
- Milman, A.S., Wilhelm, T.T., 1985. Sea surface temperatures from the scanning multichannel microwave radiometer on Nimbus 7. *J. Geophys. Res.* 90 (C6), 11631. <https://doi.org/10.1029/JC090iC06p11631>.
- Minnett, P.J., Alvera-Azcárate, A., Chin, T.M., Corlett, G.K., Gentemann, C.L., Karagali, I., Li, X., Marsouin, A., Marullo, S., Maturi, E., Santoleri, R., Saux Picart, S., Steele, M., Vazquez-Cuevo, J., 2019. Half a century of satellite remote sensing of sea-surface temperature. *Remote Sens. Environ.* 233, 111366. <https://doi.org/10.1016/j.rse.2019.111366>.
- Monzikova, A.K., Kudryavtsev, V.N., Reul, N., Chapron, B., 2017. On the upper ocean response to tropical cyclones: Satellite microwave observation. In: *Progress in Electromagnetics Research Symposium-Fall (PIERS-FALL)*. IEEE, pp. 2437–2444.
- Nielsen-Englyst, P., Hoyer, L.J., Toudal Pedersen, L.L., Gentemann, C., Alerkskans, E., Block, T., Donlon, C., 2018. Optimal estimation of sea surface temperature from AMSR-E. *Remote Sens.* 10 (2), 229. <https://doi.org/10.3390/rs10020229>.
- Ning, J., Qing, X., Wang, T., Zhang, S., 2018. Upper Ocean response to super typhoon soudelor revealed by different SST products. In: *IGARSS 2018–2018 IEEE International Geoscience and Remote Sensing Symposium*. IEEE.
- O'Carroll, A.G., Armstrong, E.M., Beggs, H.M., Bouali, M., Casey, K.S., Corlett, G.K., Dash, P., Donlon, C.J., Gentemann, C.L., Hoyer, J.L., Ignatov, A., Kabobah, K., Kachi, M., Kurihara, Y., Karagali, I., Maturi, E., Merchant, C.J., Marullo, S., Minnett, P.J., Pennybacker, M., Ramakrishnan, B., Ramsankaran, R., Santoleri, R., Sunder, S., Saux Picart, S., Vázquez-Cuevo, J., Wimmer, W., 2019. Observational needs of sea surface temperature. *Front. Mar. Sci.* 6, 420. <https://doi.org/10.3389/fmars.2019.00420>.
- Pearson, K., Merchant, C., Embury, O., Donlon, C., 2018. The role of advanced microwave scanning radiometer 2 channels within an optimal estimation scheme for sea surface temperature. *Remote Sens.* 10 (2), 90. <https://doi.org/10.3390/rs10010090>.
- Pearson, K., Good, S., Merchant, C.J., Prigent, C., Embury, O., Donlon, C., 2019. Sea surface temperature in global analyses: gains from the Copernicus imaging microwave radiometer. *Remote Sens.* 11 (20), 2362. <https://doi.org/10.3390/rs11202362>.
- Prigent, C., Aires, F., Bernardo, F., Orhac, J.-C., Goutoule, J.-M., Roquet, H., Donlon, C., 2013. Analysis of the potential and limitations of microwave radiometry for the retrieval of sea surface temperature: definition of MICROWAT, a new mission concept: sea temperature from microwaves. *J. Geophys. Res. Oceans* 118 (6), 3074–3086. <https://doi.org/10.1029/jgrc.20222>.
- Reul, N., Tenerelli, J., Chapron, B., Vandemark, D., Quilfen, Y., Kerr, Y., 2012. SMOS satellite L-band radiometer: A new capability for ocean surface remote sensing in hurricanes: SMOS L-BAND radiometer and high winds. *J. Geophys. Res.* 117 (C2) <https://doi.org/10.1029/2011JC007474> n/a-n/a.
- Reul, N., Chapron, B., Zabolotskikh, E., Donlon, C., Quilfen, Y., Guimard, S., Piolle, J.F., 2016. A revised L-band radio-brightness sensitivity to extreme winds under tropical cyclones: the five year SMOS-storm database. *Remote Sens. Environ.* 180, 274–291. <https://doi.org/10.1016/j.rse.2016.03.011>.
- Reul, N., Chapron, B., Zabolotskikh, E., Donlon, C., Mouche, A., Tenerelli, J., Collard, F., Piolle, J.F., Fore, A., Yueh, S., Cotton, J., Francis, P., Quilfen, Y., Kudryavtsev, V.,

2017. A new generation of tropical cyclone size measurements from space. *Bull. Am. Meteor. Soc.* 98 (11), 2367–2385. <https://doi.org/10.1175/BAMS-D-15-00291.1>.
- Reynolds, R.W., Rayner, N.A., Smith, T.M., Stokes, D.C., Wang, W., 2002. An improved in situ and satellite SST analysis for climate. *J. Clim.* 15 (13), 1609–1625. [https://doi.org/10.1175/1520-0442\(2002\)015<1609:AIISAS>2.0.CO;2](https://doi.org/10.1175/1520-0442(2002)015<1609:AIISAS>2.0.CO;2).
- Rodgers, C.D., 2000. *Inverse Methods for Atmospheric Sounding - Theory and Practice*. World Scientific Publishing Co. Pte. Ltd.
- Scarlat, R.C., Spreen, G., Heygster, G., Huntemann, M., Pañilea, C., Pedersen, L.T., Saldo, R., 2020. Sea Ice and atmospheric parameter retrieval from satellite microwave radiometers: synergy of AMSR2 and SMOS compared with the CIMR candidate mission. *J. Geophys. Res. Oceans* 125 (3). <https://doi.org/10.1029/2019JC015749>.
- Shibata, A., 2006. Features of ocean microwave emission changed by wind at 6 GHz. *J. Oceanogr.* 62 (3), 321–330. <https://doi.org/10.1007/s10872-006-0057-3>.
- Ulaby, F.T., Moore, R.K., Fung, A.K., 1981. *Microwave Remote Sensing: Active and Passive. Volume 1-Microwave Remote Sensing Fundamentals and Radiometry*.
- Vázquez-Cuervo, J., Armstrong, E.M., Harris, A., 2004. The effect of aerosols and clouds on the retrieval of infrared sea surface temperatures. *J. Clim.* 17 (20), 3921–3933. [https://doi.org/10.1175/1520-0442\(2004\)017<3921:TEOAAAC>2.0.CO;2](https://doi.org/10.1175/1520-0442(2004)017<3921:TEOAAAC>2.0.CO;2).
- Wentz, F.J., 2015. A 17-Yr climate record of environmental parameters derived from the tropical rainfall measuring Mission (TRMM) microwave imager. *J. Clim.* 28 (17), 6882–6902. <https://doi.org/10.1175/JCLI-D-15-0155.1>.
- Wentz, F.J., Meissner, T., 2000. *AMSR Ocean Algorithm. Algorithm Theoretical Basis Document, Remote Sensing Systems, Santa Rosa, CA*.
- Wentz, F.J., Meissner, T., 2007. Supplement 1 Algorithm Theoretical Basis Document for AMSR-E Ocean Algorithms. RSS Technical Report 051707. Remote Sensing Systems, Santa Rosa, CA [online] Available from: http://images.remss.com/papers/rsstech/2007_051707_Wentz_AMSR_Ocean_Algorithm_Version_2_Supplement1_ATBD.pdf.
- Wentz, F.J., Gentemann, C., Smith, D., Chelton, D.B., 2000. Satellite measurements of sea surface temperature through clouds. *Science* 288 (5467), 847–850. <https://doi.org/10.1126/science.288.5467.847>.
- Wilheit, T., 1979. A model for the microwave emissivity of the Ocean's surface as a function of wind speed. *IEEE Trans. Geosci. Electron.* 17 (4), 244–249. <https://doi.org/10.1109/TGE.1979.294653>.
- Woodruff, S.D., Worley, S.J., Lubker, S.J., Ji, Z., Eric Freeman, J., Berry, D.I., Brohan, P., Kent, E.C., Reynolds, R.W., Smith, S.R., Wilkinson, C., 2011. ICOADS Release 2.5: extensions and enhancements to the surface marine meteorological archive. *Int. J. Climatol.* 31 (7), 951–967. <https://doi.org/10.1002/joc.2103>.
- Yang, C.-S., Kim, S.-H., Ouchi, K., Back, J.-H., 2015. Generation of high resolution sea surface temperature using multi-satellite data for operational oceanography. *Acta Oceanol. Sin.* 34 (7), 74–88. <https://doi.org/10.1007/s13131-015-0694-8>.
- Zhang, L., Yu, H., Wang, Z., Yin, X., Yang, L., Du, H., Li, B., Wang, Y., Zhou, W., 2020. Evaluation of the initial sea surface temperature from the HY-2B scanning microwave radiometer. *IEEE Geosci. Remote Sensing Lett.* 1–5. <https://doi.org/10.1109/LGRS.2020.2968635>.